scientific reports

Check for updates

OPEN

DFT-based exploration of pressure effects on the physical properties of Zinc-blende materials XM (X = Ga, In; M = As, N) for optoelectronic devices

Maahi Sabah[1], Ahmad Irfan[2], Md. Saiful Islam[1,4], Md. Tanvir. Ahmed[1,4], Ruma Parvin[3], Md. Atikur Rahman[1]✉ & Md. Shahajan Ali[1]✉

Physical properties of *XM* (*X* = Ga, In; *M* = As, N) were studied under hydrostatic pressure based on DFT simulation. The phonon calculations reveal the dynamical stability of all compounds by demonstrating no imaginary lines. Stiffness constants preserved the Born's constancy and assured the mechanical steady nature. However, the significant variations of elastic parameters under pressure indicate possible phase change for InN at 6 GPa, GaN 6 ± 2 GPa and InAs at 8 GPa, respectively. The analysis of electronic band structures reveal semiconducting attitude of the materials investigated in the range of 0.4 eV to 3.2 eV which are suitable for optoelectronic device applications. According to Pugh's and Pettifor's condition, GaAs exhibits brittle to ductile at 4 GPa wherever the other phases display ductile activities at 0 GPa to high pressure. Apart from the material GaN, the other phases show very soft manner according to Vickers hardness exploration. The refractive index and static dielectric function of the compounds show excellent alignment with previously reported available data. High values in dielectric function ensure the probable applications for manufacturing high value capacitors. Among the materials analyzed GaN shows the lowest thermal expansion coefficient at equilibrium conditions, representing the maximum stiffness to deformation. The increase trend of Debye temperature with pressure ensures the materials converted to more thermal conductive.

Keywords Zinc blende semiconducting structure, Phonon dynamics, Mechanical features, Electronic properties, Optical and thermal properties

The III–V group compounds, specifically *XM* (*X* = Ga, In and *M* = N, As), have garnered significant attention due to their pivotal role in advanced scientific applications. These binary octet compounds, classified as ANB8 – N types, are instrumental in the fabrication of heterostructures and tunable devices operating within the visible spectrum. They are extensively utilized in optoelectronic technologies, particularly in high-frequency applications, owing to their remarkable combination of properties, including wide band gaps, exceptional charge carrier mobility, and band gap versatility, which are crucial for innovations in LEDs, lasers, and other cutting-edge devices[1–6]. The operating characteristics of electronic and optoelectronic devices extend beyond practical materials engineering, offering deeper insights into the intrinsic properties of materials and the fundamental science underlying them. Both theoretical and experimental investigations are indispensable for advancing research in this field, as they provide critical frameworks for understanding the behavior of complex systems. These systems, encompassing diverse compound semiconductors, have garnered immense interest in both fundamental and applied physics. Such research not only enriches our theoretical comprehension of these materials but also underpins their practical integration into cutting-edge technologies, bridging the gap between fundamental science and transformative applications[7–18].

[1]Department of Physics, Pabna University of Science and Technology, Pabna 6600, Bangladesh. [2]Department of Chemistry, College of Science, King Khalid University, P.O. Box 9004, Abha 61413, Saudi Arabia. [3]Department of Physics, University of Rajshahi, Rajshahi 6205, Bangladesh. [4]Theoretical and Experimental Advanced Materials Science Lab (TEAMS), Pabna University of Science and Technology, Pabna 6600, Bangladesh. ✉email: atik0707phy@gmail.com; msali@pust.ac.bd

The exploration of these semiconductor materials under high-pressure conditions has become a highly active area of research. Pressure exerts a profound influence on the chemical and physical properties of matter, often inducing the emergence of novel crystal phases and unique behaviors. Additionally, the capability to investigate structural stability as a function of volume introduces a fresh perspective to the fundamental relationship between atomic and electronic structures. This progress has unlocked new frontiers in solid-state physics and crystallography, enabling deeper insights into material behavior at extreme conditions[19–21]. These advancements have unveiled numerous fascinating possibilities in the field of condensed matter physics. The investigation of transformations in crystallographic phases alongside the mechanical and electronic properties of materials under pressure, has garnered growing interest from both experimentalists and theoreticians alike. The semiconductors (GaAs, InAs, GaN, and InN) are vital in shaping the evolution of microwave, optoelectronic, and electronic devices. They form the foundation spanning numerous types of both established commercial applications and emerging technologies, including light-emitting diodes, integrated circuits, photo detectors, lasers, filters, and modulators. Belonging to the family of common-anion III-V semiconductors, III-arsenide compounds are notable for their extensive energy gap range, surpassed only by III-nitrides. Under standard conditions, the studied III-V semiconductors—GaAs, InAs, GaN, and InN—crystallize in the zinc blende[22–24].

As these semiconductors of both arsenide and nitride materials are direct band gap semiconductors, they're used for the construction of infrared detectors, for the wavelength range of 1–3.8 μm. The detectors are usually photovoltaic photodiodes[25]. In 1994, a first-order phase transition was observed from the zinc blende (B3) structure to the NiAs (B8) structure at an equilibrium transformation pressure of 7 ± 5 GPa.(26) Greene et al.[26] reported that AlAs undergoes a transformation from the zinc-blende to the NiAs structure at 7.5 GPa. In contrast, Weir et al.[27] observed that GaAs exhibits complex phase behavior under pressure, transitioning from the zinc-blende (GaAs-I, space group $F\bar{4}3m$) structure to an orthorhombic (GaAs-II) phase, with a proposed space group of Pmm2[27]. This orthorhombic phase is considered a distortion of the B1 (space group Fm-3 m) phase[28–30]. The transition pressure was initially found to be around 17 GPa[26], but recent results suggest a transition pressure of approximately 12 ± 1.5 GPa[31]. The high-pressure phases of InAs have been experimentally determined by Vohra et al.[32], who observed a transformation from the zinc-blende (InAs-I) structure to the rock-salt (InAs-II) phase at 7 ± 0.2 GPa, followed by a further transition to the InAs-III phase at 17 ± 0.4 GPa. InAs-III is recognized as the tetragonal phase of the β-tin type. In 2016, the structural, elastic, thermodynamic, electronic, and optical properties of four predicted novels (*Pmn21-AlN*, *Pbam-AlN*, *Pbca-AlN and cmcm-AlN*)—were calculated in detail using first-principles methods[33]. In 2017 H. Qin et al.. studied the mechanical, thermal as well as electronic features of GaN[34]. A. F. Wright investigated the elastic properties of AlN, GaN and InN at ambient condition[35]. Dinesh Chandra Gupta and Subhra Kulshrestha examined the high pressure effect on polymorphic phase transition and electronic structure of XAs (X = Al, Ga, In) in 2010[1]. Z. Zhang et al.. studied the physical properties of III–V compounds AlN, GaN, AlP, and GaP in the P3121 phase[36]. The phonon dispersion curves of AlN, GaN, and InN have been carried out by Bungaro et al.. through the *ab*-initio method[37]. Although numerous theoretical studies on the physical properties of GaAs, InAs, GaN, and InN exist in the literature, the effects of pressure on various properties of these materials remain insufficiently explored. Therefore. The main focus of this research is to explore the pressure effect on the physical properties of *XM* (*X* = Ga, In; *M* = As, N) through hypothetical ab-initio method. Theoretical studies of III-arsenide compounds have employed a diverse array of methods, spanning from phenomenological approaches like k·p theory, where the symbol k represents the electron wave vector in reciprocal space, p denotes the momentum operator and empirical pseudopotential techniques[38] to more advanced atomistic ab initio methods. This study employs a combination of advanced first-principles approaches, including the full-potential linearized augmented plane wave (FP-LAPW) method commonly implemented within the frameworks generalized gradient approximation (GGA) alongside pseudopotential techniques[39]. In this research, we explore the structural characteristics, pressure-induced mechanical stability, electronic band configurations, optical as well as thermal responses of cubic *XM* (*X* = Ga, In; *M* = N, As) compounds. Building on this foundation, the work delivers a systematic, cross-validated assessment of pressure effects reducing methodological bias in derived properties. It quantifies how hydrostatic compression alters electronic structure, effective masses and optical spectra, offering predictive guidance for strain-engineered optoelectronic devices and high-pressure sensor applications. Finally, by correlating mechanical stability with changes in electronic and thermal behavior, the study provides a unified framework that informs both fundamental understanding and practical materials selection under extreme conditions.

Computational methods

In this work, we have employed both CASTEP and WIEN2k two state-of-the-art first-principles simulation packages based on distinct DFT methodologies to ensure methodological robustness and computational accuracy. The structural, elastic, electronic, optical and thermal properties of *XM* (*X* = Ga, In; *M* = N, As) were analyzed using the Cambridge Serial Total Energy Package (CASTEP)[40–43]. For electronic exchange-correlation, the generalized gradient approximation (*GGA*) was employed, following the PW-91 scheme[43]. Ultrasoft pseudopotentials were utilized to model all ion-electron interactions in these calculations. The total energies computed within the DFT framework often exhibit sufficient accuracy to reliably predict structural stability[44]. The accuracy of calculated properties largely depends on two critical parameters: the cutoff energy and the k-point grid used in the computations. An energy cut-off of 520 eV was consistently employed across all studied compounds to ensure reliable plane-wave expansion of the wavefunctions. For precise Brillouin zone integration and uniform sampling across the reciprocal space directions, the Monkhorst-Pack scheme[45] was implemented. A meticulously optimized k-point mesh of 12 × 12 × 12 was utilized, as it demonstrated excellent convergence behavior and yielded the minimum total energy, thereby ensuring an accurate representation of the

electronic structure within the Brillouin zone. Total-energy changes between ionic steps were required to be ≤ 5×10^{-5} eV/atom, with maximum residual forces ≤ 0.10 eV·Å^{-1}, pressure tolerance ≤ 0.20 GPa, and maximum atomic displacements ≤ 0.005 Å; electronic self-consistency was enforced to 1.0×10^{-5} eV/atom for all SCF cycles. The ground-state structural parameters were obtained using the Broyden–Fletcher–Goldfarb–Shanno (BFGS) minimizer[46,47]. Elastic constants (*C*ij) for these compunds were derived via the stress–strain method with a maximum strain amplitude of 0.003. Convergence criteria for the elastic-constant calculations were set to a total-energy tolerance of 1×10^{-6} eV/atom, a maximum force threshold of 0.002 eV·Å^{-1}, and a maximum atomic displacement of 1×10^{-4} Å. For each applied strain state, four incremental steps were used to evaluate the resulting stresses. Hydrostatic pressure was applied by imposing an external pressure, performing variable-cell relaxations at discrete pressure increments up to the maximum investigated pressure. We have employed Density Functional Perturbation Theory (DFPT) within the plane-wave pseudopotential framework of CASTEP to model phonon behavior and material responses to electric fields[40,48]. This approach leverages norm-conserving pseudopotentials (NCPs) and utilizes Fast Fourier Transform (FFT) grids to ensure a consistent treatment of incommensurate lattice perturbations. Central to our method is the calculation of the first-order exchange-correlation potential in the GGA, meticulously adapted for FFT grid compatibility. We further enhanced efficiency by integrating a conjugate-gradient solver, preconditioned to include all electronic bands, for the self-consistent variational minimization of the second-order total energy[49]. To strengthen the reliability of our electronic structure analysis, the total density of states (TDOS) was computed using both CASTEP and WIEN2k, enabling a comparative assessment across different DFT implementations. In contrast, electronic band structure and band gap evaluations were carried out solely within the WIEN2k framework. These WIEN2k-based calculations were initially computed *FP-LAPW + lo* method as implemented in the WIEN2k code[50], which is known for its high precision in electronic structure calculations, particularly near the Fermi level. To enhance the accuracy of the band gap predictions, we subsequently repeated the same calculations employing the modified Becke–Johnson exchange potential combined with local density approximation (mBJ-LDA)[51], as incorporated in the WIEN2K 2011 code. The mBJ-LDA functional is specifically designed to yield improved band gap estimations for semiconductors and insulators, making it highly suitable for this study. Numerical parameters were set to ensure robust convergence where RKmax = 8, the energy convergence criterion (EC) = 0.0001 Ry, and the charge convergence (CC) = 0.01 e. SCF cycles were considered converged when the change in total energy between successive iterations fell below 0.01 mRy. The purpose of selecting the muffin tin radii (RMT) was to minimize the interstitial gap and ensure nearly touching spheres. The expansion of the wave functions was set to *l*max = 8 inside the muffin tin spheres, and the charge density was Fourier expanded up to *G*max = 12 (a.u.)-1, where *G*max is the parameter that, in charge density Fourier expansion, sets the magnitude of largest vector to 14. The number of plane waves was calculated using RMT×*K*max = 8. Final RMT adjustments (reductions from initial estimates) were: GaAs 8.2%, InAs 10.0%, GaN 5.3%, and InN 4.3% to ensure numerical stability and consistent basis completeness Band structures were computed along high-symmetry directions of the cubic Brillouin zone sampled with sufficiently dense k-paths to resolve band extrema.

Results and discussion

Structural properties

Gallium arsenide (GaAs), indium arsenide (InAs), gallium nitride (GaN) and indium nitride (InN), are considered in the zinc-blende structure, crystallizing in the cubic $F\bar{4}3m$ space group (216). In this structure, the materials consist of two face-centered cubic (FCC) sub-lattices offset by half the diagonal of the unit cell. Each cation (Ga^{3+} or In^{3+}) is tetrahedrally bonded to four anions (As^{3-} or N^{3-}), forming corner-sharing tetrahedra, while each anion is similarly bonded to four cations, creating corresponding corner-sharing tetrahedra. For GaAs, the Ga-As bond length is uniformly 2.46 Å at 0 pressure. The equilibrium lattice parameter with geometry optimization has a value of 5.67641 Å. The lattice constant of InAs is 6.120687Å, slightly larger than that of GaAs due to the larger ionic radius of indium, and the In-As bond length reflects this increased lattice parameter. Gallium nitride (GaN) and indium nitride (InN) are typically found in the hexagonal $P6_3mc$ space group, which is more common for these materials. However, in this study, the zinc-blende structure has been considered for both compounds. The lattice parameters used in the calculations are 4.515 Å and 5.0359 Å, for GaN and InN respectively, which correspond to a relatively compact crystal structure. For GaN, Ga-N bond length is uniformly 1.955 Å, shortest among all four compounds whereas for InN, In-N bond of 2.18 Å is observed. The bond lengths also suggest slight deviations from perfect tetrahedral coordination, which is typical in this material. The position of Ga and In atoms are at (0, 0, 0), and As and N atoms are at (1/4, 1/4, 1/4). The optimized crystal structure of the GaAs compound is illustrated in Fig. 1, with its two-dimensional and three-dimensional representations depicted in panels (a) and (b), respectively. In these cubic crystal structures, the lattice parameters follow $a = b = c$ and $\alpha = \beta = \gamma = 90°$. The calculated lattice parameter, $a_{0,}$ unit cell volume V_0 and bond length for GaAs, InAs, GaN, and InN are presented in Table S1, alongside existing experimental and theoretical values.

Figure 2(a) shows that the unit cell volume, *V* of GaAs, InAs, GaN, and InN systematically decreases under pressure. This reduction in volume arises because external pressure strengthens atomic bonding, leading to a contraction in lattice dimensions. As shown in Fig. 2(b), the lattice parameters also decrease with increasing hydrostatic pressure, reflecting enhanced atomic interactions that reduce interatomic spacing.

Similarly, Fig. 2(c) demonstrates a smooth decrease in bond length for all four compounds. These structural compressions directly influence the mechanical response, shorter bonds and reduced volume increase the stiffness of the crystal, which is reflected in the rising elastic constants and moduli with pressure. The strong correlation between structural contraction and mechanical strengthening highlights how pressure not only stabilizes the lattice but also governs its elastic behavior.

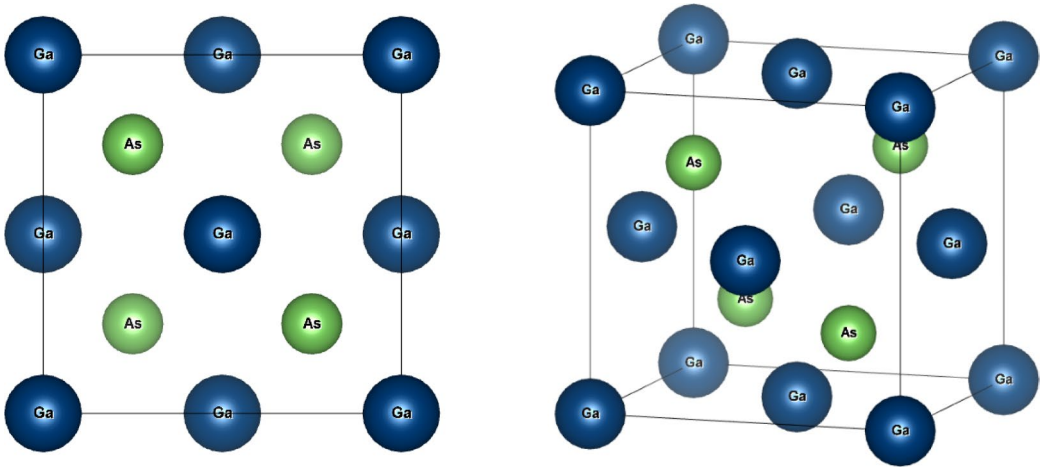

Fig. 1. 2D and 3D view of the crystal structure of Ga-As cubic cell.

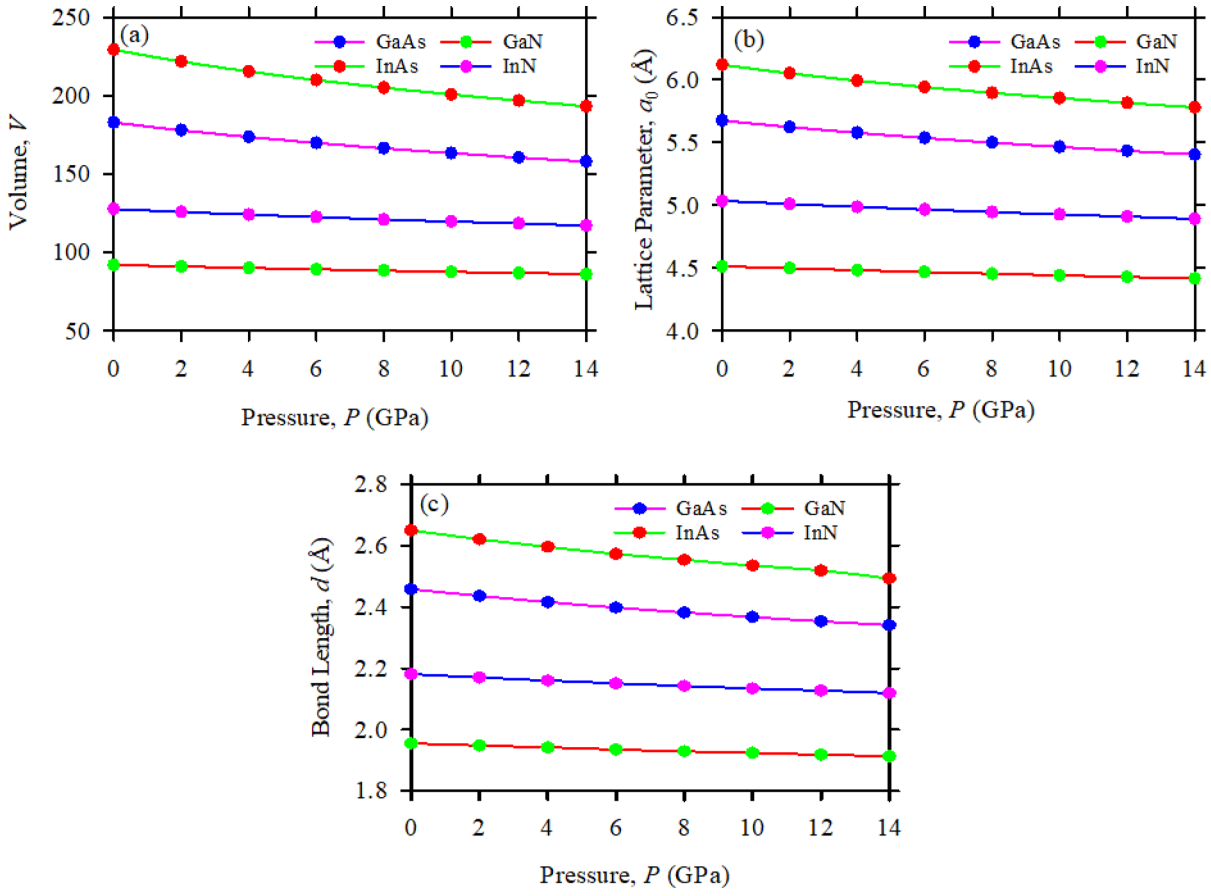

Fig. 2. Variation of **(a)** Volume, V **(b)** Lattice parameter a_0, and **(c)** Bond length d with pressure for GaAs, InAs, GaN and InN.

Phonon dynamics

The characteristics of phonons play a pivotal role in solid-state physics, as they significantly affect both thermal and electronic transport phenomena. Phonon behavior directly determines a crystal's dynamical and structural stability. The nature of phonon modes is essential for understanding how atoms interact and vibrate within the lattice. A wide range of material properties thermal, mechanical, and electronic can be assessed either directly or indirectly through phonon dispersion spectra (PDS) and phonon density of states (PHDOS)[53]. These dispersion curves serve as crucial indicators of a material's dynamical robustness, potential structural phase transitions,

and the extent to which atomic vibrations contribute to thermal conductivity and related properties[54]. In the present study, to evaluate dynamical stability, the phonon dispersion relations for GaAs, InAs, GaN, and InN were computed at absolute zero temperature.

The resulting phonon spectra are interpreted via the harmonic approximation, which hinges on the force-constant matrix as the primary descriptor of lattice vibrations. The defining equation for this tensor, denoted $D_{\nu\mu}$, reads:

$$D\nu\mu = \frac{\partial^2 E}{\partial u_\nu \partial u_\mu} \tag{1}$$

where E is the total crystal energy and u_ν, u_μ are atomic displacements evaluated at the equilibrium positions[55,56].

From Fig. 3 (a-d), the phonon dispersion spectra for GaAs, InAs, GaN, and InN, exhibit no imaginary (negative) frequencies across the entire Brillouin zone, unequivocally demonstrating the dynamical stability of all four compounds at equilibrium. The three acoustic branches (two transverse and one longitudinal) emanate linearly from zero frequency at the Γ point and reach on the order of around 3, 2, 9 and 4 THz for GaAs, InAs, GaN, and InN respectively at the Brillouin-zone edges. Above the acoustic bands lie twenty-one optical branches: longitudinal optic (LO) and transverse optic (TO). The highest phonon optical modes occur around 8 THz for GaAs and InAs, in contrast, GaN and InN extend up to approximately 20 THz, reflecting the presence of lighter nitrogen atoms and stronger atomic bonds. The phonon dispersion curve at 6 GPa and 14 GPa for all four compounds are shown in Fig. 1S which have no negative value confirming their dynamical stability throughout the pressures. From the PDOS analysis in Fig. 3 (c, d), a clear separation is observed between the atomic contributions in both GaN and InN. The heavier Ga and In atoms predominantly influence the low-frequency modes, while the lighter N atoms are primarily responsible for the high-frequency optical modes. This results in Ga and In dominating the acoustic region, whereas N contributions are concentrated in the optical domain. Notably, some optical modes overlap with the acoustic range, but the higher-frequency optical modes are distinctly isolated by a gap between the lower-frequency vibrations.

Now, considering the PDOS profiles shown in Fig. 3(a, b), GaAs shows comparable contributions from Ga and As across both low- and high-frequency optical modes due to their similar atomic masses, while in InAs, In contributes more to the lower-frequency modes and As to the higher ones. This behavior has meaningful

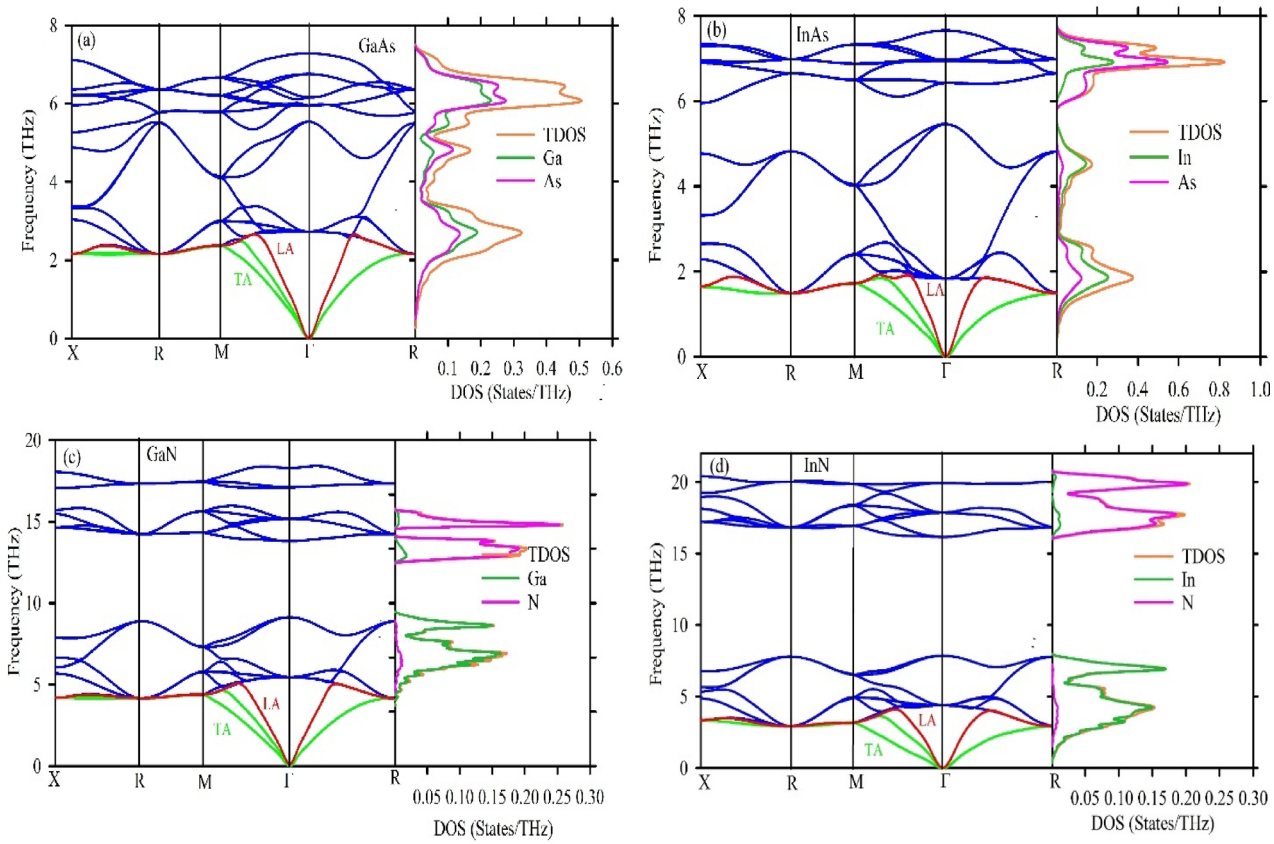

Fig. 3. The Phonon dispersion curve and phonon density of states for the **(a)** GaAs, **(b)** InAs **(c)** GaN and **(d)** InN at 0 GPa.

implications for thermal and mechanical properties: the high-frequency optical phonons in GaN and InN suggest more resilient lattice dynamics. Conversely, the lower-frequency optical modes in GaAs and InAs are characteristic of III–V semiconductors commonly employed in optoelectronic devices, where phonon scattering particularly LO phonons plays a significant role in carrier mobility and thermal performance.

Mechanical properties

The elastic stiffness of a material is intricately connected to its physical properties, including brittle Type equation here.ness, ductility, mechanical stability, and overall stiffness. These fundamental attributes play a crucial role in defining the material's mechanical behavior[57]. Understanding the elastic properties is essential to elucidate the material response under external stresses. Furthermore, the interatomic connectivity and its implications for their neighbors, as well as the material's cohesive forces, can be inferred from the study of elastic stiffness[58]. Thus, investigating the elastic constants is of paramount importance to gain deeper insights into the material's structural and mechanical integrity. The calculated elastic constants for GaAs, InAs, GaN, and InN under varying pressure conditions are listed in Table 1. To assess the mechanical stability of these cubic materials under isotropic pressure, the Born's criteria[59] are applied:

Compounds	*P*	C_{11}	C_{12}	C_{44}	B	G_v	G	E	υ	B/G	G_v/B	Ref
GaAs	0	108.3	49.5	57.6	69.1	46.3	44	108.8	0.237	1.57	0.670	*a**
		106.5	53.3	60.2	75.5	----	32.6	85.5	----	2.32	----	62
	2	117.6	58.1	64.0	77.9	50.3	47.1	117.5	0.248	1.65	0.645	
	3	122.5	62.8	65.8	82.7	51.4	47.9	120.4	0.257	1.73	0.622	
	4	127.3	67.5	67.4	87.4	52.4	48.6	123.1	0.265	1.80	0.599	
	6	136.3	76.7	69.9	96.6	53.8	49.7	127.2	0.280	1.94	0.558	
	8	144.6	85.3	72.0	105	55.1	50.4	130.4	0.293	2.09	0.524	*a**
	10	152.3	93.5	74.1	113	56.2	51.1	133.3	0.303	2.21	0.497	
	12	160.1	102	75.3	121	56.8	51.4	135.1	0.314	2.36	0.468	
	14	167.5	110.2	76.2	129	57.1	51.5	136.3	0.324	2.51	0.442	
InAs	0	80.3	46.1	46.3	57.5	34.7	31.1	79.1	0.271	1.85	0.603	*a**
		83	45	40	48.8	----	29.6	73.4	----	1.65	----	34
	2	88.8	55.8	48.3	66.8	35.6	31.4	81.5	0.297	2.13	0.532	
	4	96.9	65.5	48.9	76.0	35.7	31.1	82.1	0.320	2.44	0.469	
	6	104.0	74.3	49.5	84.2	35.7	30.7	82	0.338	2.74	0.423	
	8	110.8	82.9	48.2	92.2	34.5	29.4	79.8	0.356	3.14	0.375	*a**
	10	117.8	91.8	47.4	100	33.7	28.4	77.7	0.371	3.54	0.335	
	12	124.5	100.5	43.2	108	30.7	26.0	72.2	0.389	4.17	0.283	
	14	130.8	108.8	42.4	116	29.9	24.8	69.6	0.400	4.69	0.257	
GaN	0	260.7	143.4	155.6	182	116.9	105.3	264.9	0.258	1.73	0.640	*a**
		286.9[1],249[2]	152, 127	165, 151	199, 168	----	113,105	285.3,260	0.26,0.242	1.76,1.60	----	351362
	1	264.7	148	157.4	186	117.8	105.8	267.0	0.262	1.77	0.630	
	2	269.8	152.6	158.7	191	118.7	106.5	269.5	0.266	1.80	0.619	
	4	334.0	167.8	160.3	222	129.4	123.2	312.1	0.267	1.81	0.580	
	6	330.5	177.4	162.0	228	127.9	120.0	306.3	0.277	1.90	0.560	
	8	289.6	178.4	164.9	215	121.2	106.8	274.9	0.287	2.02	0.562	*a**
	10	296.4	186.5	162.1	223	119.3	105.2	272.7	0.296	2.12	0.534	
	12	303.7	195.5	163.9	231	120.0	105.2	274.1	0.303	2.20	0.518	
	14	310.5	204	164.8	239	120.2	105	274.8	0.309	2.28	0.502	
InN	0	156.1	102.9	88.1	120	63.5	54.7	142.5	0.303	2.21	0.527	*a**
		187	125	86	137	----	-----	162.1[58]	----	2.11	----	35
	2	163.8	112.6	89.5	129	64.0	54.4	143.2	0.316	2.38	0.494	
	4	171.3	122.1	90.4	138	64.1	53.9	143.1	0.328	2.57	0.463	
	6	178.1	131.3	89.5	146	63.1	52.6	140.9	0.340	2.79	0.429	
	8	185.6	140.7	88.6	156	62.2	51.5	139.1	0.351	3.02	0.399	*a**
	10	192.3	149.8	88.6	164	61.7	50.4	137.2	0.361	3.25	0.376	
	12	199.0	158.6	88.4	172	61.2	49.4	139.2	0.369	3.48	0.355	
	14	205.6	167.6	88.3	180	60.6	48.3	132.9	0.377	3.73	0.336	

Table 1. Calculated elastic constants, C_{ij} (GPa), polycrystalline bulk modulus B (GPa), shear modulus G (GPa), young's modulus E (GPa), poisson's ratio ν, pugh's ratio (B/G), pettifor criterion (G_v/B) for XM at different pressures. *a** represents present work .

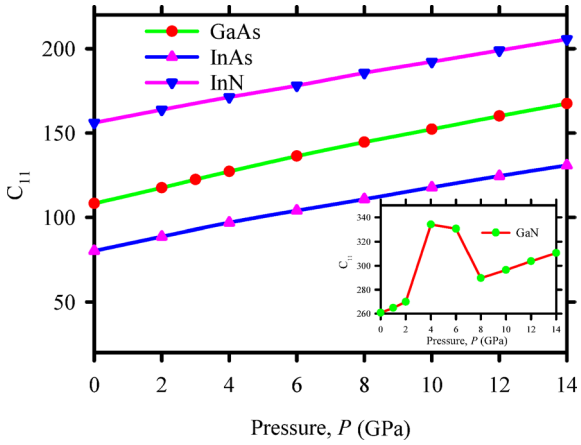

Fig. 4. Pressure dependence elastic constant C_{11} for (a) GaAs, (b) InAs, (c) GaN (inside the figure), and (d) InN.

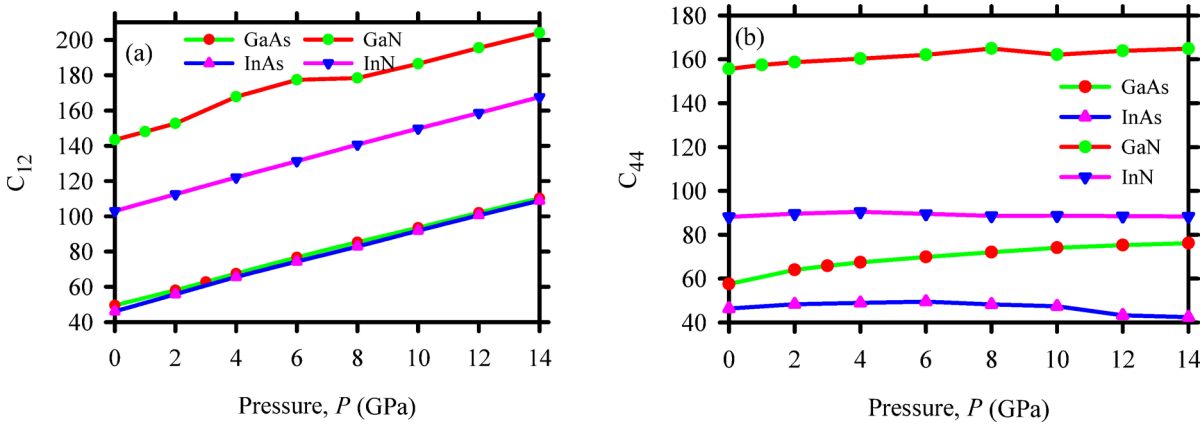

Fig. 5. Pressure dependence elastic constant C_{12} for **(a)** GaAs, InAs, GaN and InN and C_{44}**(b)** for GaAs, InAs, GaN and InN.

$$C_{11} > 0, C_{44} > 0, C_{11} - C_{12} > 0 \text{ and } C_{11} + 2C_{12} > 0 \tag{2}$$

And also at higher pressure mechanical stability is ensured by[60,61]:

$$\widetilde{C}_{11} - \widetilde{C}_{12} > 0, \widetilde{C}_{11} + 2\widetilde{C}_{12} > 0, \text{ and } \widetilde{C}_{44} > 0 \tag{3}$$

Where,

$$\widetilde{C}_{11} = C_{11} - \mathrm{P}, \widetilde{C}_{12} = C_{12} + \mathrm{P}, \widetilde{C}_{44} = C_{44} - \mathrm{P} \tag{4}$$

From Table 1, it is evident that the computed elastic constants conform to the requisite stability conditions across all pressures, confirming the mechanical stability of the materials. Elastic constants serve as fundamental indicators of the mechanical behavior of these materials. The C_{11} measures the resistance to longitudinal deformation under hydrostatic pressure, C_{44} reflects shear deformation resistance, and C_{12} corresponds to strain response along perpendicular axes.

The values of C_{11}, as observed in Fig. 4 (a-d), are increasd linearly with pressure for GaAs, InAs, and InN, reflecting enhanced bonding strength under compression. However, for GaN, C_{11} increases linearly up to 2 GPa, after which it exhibits anomalous behavior at 4 GPa, marked by a sudden and significant rise to an unusually high value, and then shows a noticeable drop at 6 GPa. This drop in C_{11} suggests a weakening of longitudinal bonding strength in GaN, potentially indicating the onset of structural instability or a phase transformation.

Figure 5(a) and (b) illustrate the pressure-dependent behavior of the elastic constants C_{12} and C_{44}, respectively, for GaAs, InAs, GaN, and InN. As depicted in Fig. 5(a), C_{12} exhibits an almost linear increase with pressure for GaAs, InAs, and InN, indicating a consistent stiffening of the interatomic bonding under compression. GaN,

however, demonstrates slight anomalies at 4 GPa and 6 GPa, suggesting subtle structural or bonding irregularities under these specific pressure conditions.

Meanwhile, in Fig. 5(b), InN displays indications a disruption in the steady rise of C_{44} near 4 GPa, while InAs shows a similar anomaly around 6 GPa. Although the increment is relatively modest, minor discontinuities are observed in InAs, GaN, and InN, which may be attributed to subtle changes in shear resistance or phase behavior. Nevertheless, these deviations remain minimal and do not significantly alter overall trend.

In order to elucidate the underlying mechanical characteristics, we calculate the bulk modulus (B), shear modulus (G), Young's modulus (E), and Poisson's ratio (v) using the Voigt, Reuss, and Hill approximations[65] and the bulk modulus (B_R) and shear modulus (G_R) in the Reuss (R)[66-67] approximation. The results are presented in Table 1. The mechanical properties of GaAs, InAs, GaN, and InN under hydrostatic pressure exhibit distinct trends, as illustrated in Fig. 6(a-d).

For GaAs, the bulk modulus (B), Young's modulus (E) and shear modulus (G) are increased with pressure, indicating that the material becomes stiffer and more resistant to both axial and shear deformations. This suggests a strong bond-strengthening effect under compression. In contrast, as observed in Fig. 6(b), InAs and InN exhibit a different trend—while their Young's modulus initially increases and then decreases, in Fig. 6(c) their shear modulus consistently decreases with pressure. This implies that although these materials initially become stiffer in terms of elastic deformation, beyond a certain pressure threshold, structural modifications or bond weakening reduce their ability to resist deformation.

The Zener anisotropy factor is a key parameter to quantify the extent of elastic anisotropy exhibited by solid materials[68]. A perfectly isotropic material has an anisotropy factor of unity, while deviations from this value indicate the presence of anisotropy. The calculated values of A for GaAs, InAs, GaN, and InN under 0–14 GPa pressure are presented in Fig. 6(d). Notably, the anisotropy factor (A) increases for GaAs, InAs, and InN, regardless of their initial anisotropic nature. This suggests that pressure enhances the directional dependence of their elastic properties, making them structurally more anisotropic over time.

Among all the compounds, GaN exhibits highly anomalous and discontinuous behavior across all properties, which strongly suggests pressure-induced phase transitions or structural instabilities. Alternatively, such behavior may arise from electronic and bonding rearrangements that lead to significant mechanical property fluctuations.

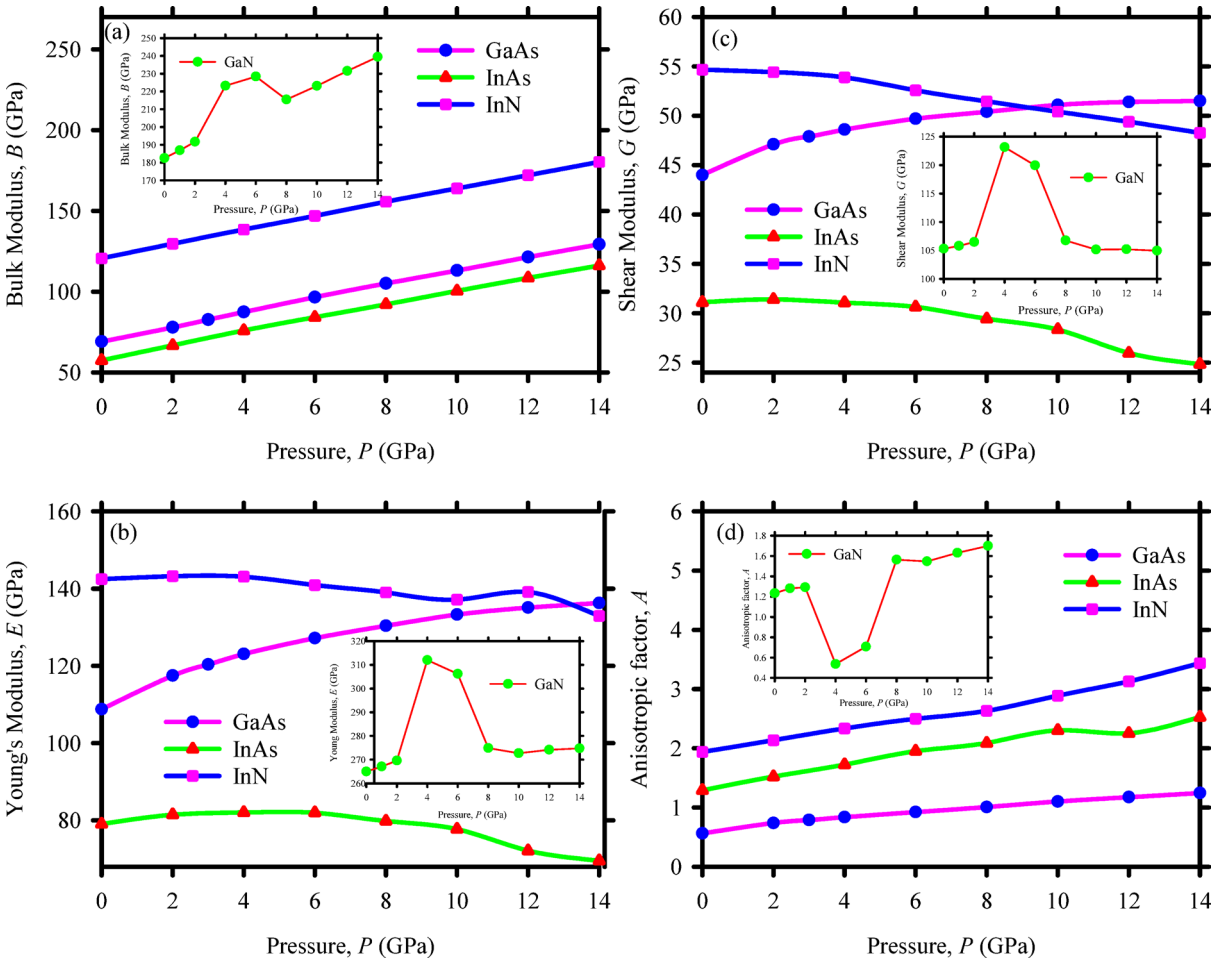

Fig. 6. **(a)** Bulk modulus, B**(b)** Young's Modulus, E**(c)** Shear modulus, G and **(d)** Anisotropic factor, A of GaAs, InAs, GaN, InN under pressure.

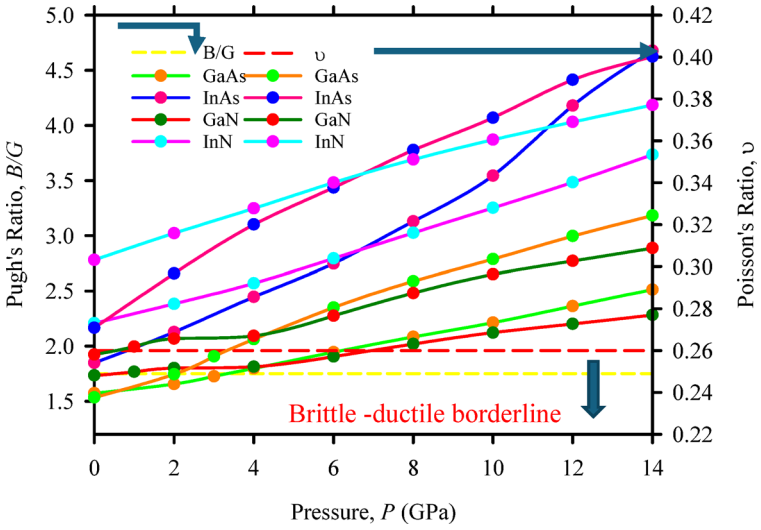

Fig. 7. Pugh's ratio and Poisson's ratio under pressure for GaAs, InAs, GaN, InN.

Compounds	*P* (GPa)	β	H_V^G (GPa)	H_V^B (GPa)	H_V^E (GPa)	Anisotropic factor, A
GaAs	0	0.014	4.88	6.65	6.60	0.562
	14	0.008	6.20	12.45	8.27	1.244
InAs	0	0.017	2.60	5.54	4.80	1.291
	14	0.009	1.49	11.19	4.22	2.529
GaN	0	0.005	15.73	17.58	16.08	1.234
	14	0.004	15.67	23.07	16.68	1.699
InN	0	0.008	6.77	11.62	8.65	1.938
	14	0.006	5.64	17.36	8.07	3.439

Table 2. Calculated compressibility β, Vickers hardness and anisotropic factor, A of GaAs, InAs, GaN, and inn at 0 and 14 GPa pressures.

The presence of these discontinuities highlights the complexity of GaN's response to pressure, distinguishing it from the other three compounds.

Additionally, the bonding nature of the materials can be inferred from Poisson's ratio. A value of $\nu \approx 0.1$ corresponds to covalent bonding, while $\nu = 0.25$ indicates ionic bonding. For ionic crystals, central force crystals exhibit ν between 0.25 and 0.50, while non-central force crystals fall outside this range[68]. In this study, the calculated ν values for all materials under pressure (0.23–0.38) suggest central force bonding.

The brittle or ductile nature of the materials was analyzed using Poisson's ratio (ν) and Pugh's criterion (B/G). Poisson's ratio $\nu < 0.26$ indicates brittleness, while $\nu > 0.26$ suggests ductility[69]. Figure 7, indicates that at 0 GPa, GaAs exhibits brittle behavior but transition to ductile nature at 4GPa, consistent with the $B/G > 1.75$ threshold of Pugh's criterion[70]. GaN is positioned just below ductile-brittle borderline at 0 GPa. InAs and InN remain ductile throughout the pressure range, as both ν and B/G exceed the respective thresholds.

These transitions are further evidenced by the conditions $C_{11} - C_{12} > 0$ and $\frac{G_v}{B} > 0.6$, which are based on Pettifor's criterion. Pettifor's criterion is used to predict the likelihood of phase transformations in materials. It suggests that when $C_{11} - C_{12}$ becomes negative, mechanical instability is signaled. Additionally, the ratio $\frac{G_v}{B}$ is also crucial in this analysis. When $\frac{G_v}{B} > 0.6$, the material tends to behave in a brittle manner, whereas a ratio of $\frac{G_v}{B} < 0.6$, typically indicates ductile behavior.

From the data in Table 2; Fig. 8, GaAs approaches $C_{11} - C_{12} = 0$ and $\frac{G_v}{B}$ values are above 0.6 at 4 GPa, indicating brittle behavior below these pressures, while materials such as InAs and InN remain ductile with $\frac{G_v}{B}$ values below 0.6. These findings provide valuable insights into the pressure-dependent mechanical stability and bonding characteristics of these materials.

Vickers hardness is a crucial mechanical property that provides insight into the plastic deformation resistance of a material under pressure. It serves as a key indicator of a material's mechanical strength, where lower hardness values correspond to softer materials, while higher values signify harder materials. The hardness of a compound can be estimated using its Bulk modulus (B), Shear modulus (G), and Young's modulus (E). According to Teter[70], the Vickers hardness can be estimated, while alternative empirical relationships have also been proposed by Jiang et al.[71-72]. The calculated hardness values for GaAs, InAs, GaN, and InN under varying pressures are presented in Table 2; Fig. 9 (b). GaAs exhibits a moderate increase in hardness with pressure due to its rising bulk and shear

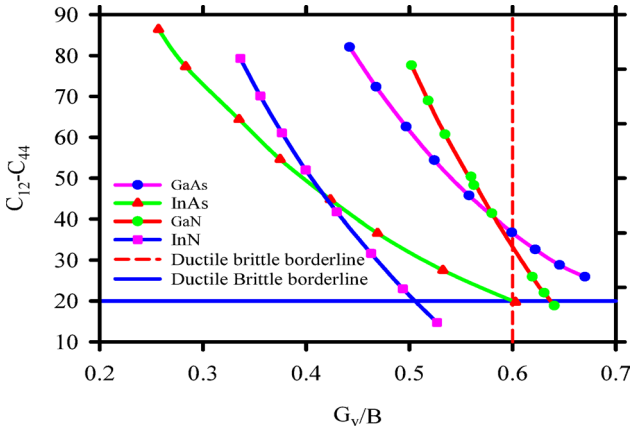

Fig. 8. Correlation between C" = (C_{12}–C_{44}) and *Gv*/*B* of *XM* (*X* = Ga, In; *M* = N, As) under pressure.

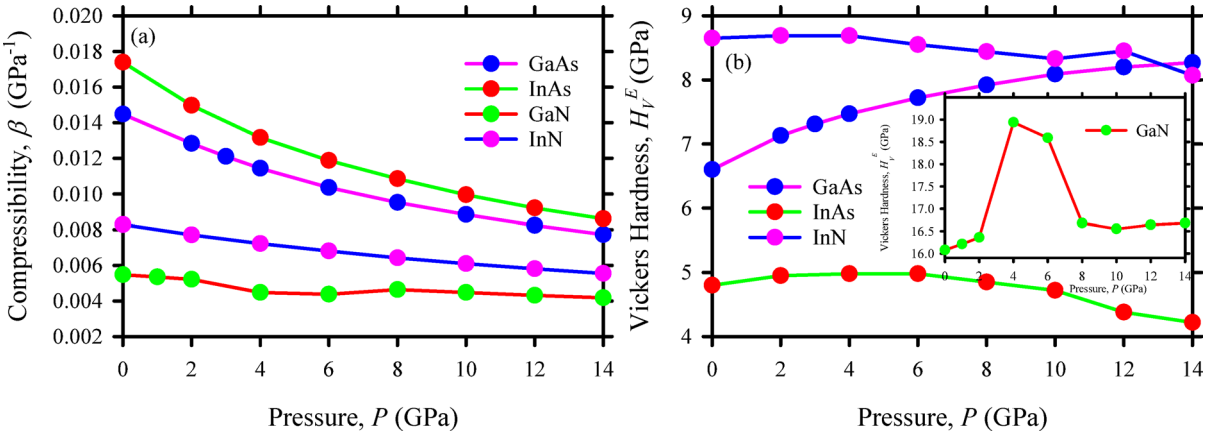

Fig. 9. **(a)** Compressibility and **(b)** hardness of GaAs, InAs, GaN, and InN under pressure.

modulus. InAs and InN, however, show non-monotonic hardness trends, reflecting their fluctuating Young's modulus and declining shear modulus. The material GaN, known for its exceptional hardness among these materials exhibits anomalous and discontinuous behaviors under pressure, potentially indicating structural transformations or electronic transitions. These variations highlight the diverse mechanical responses of III-V semiconductors under compression, emphasizing the role of bonding characteristics in determining hardness.

These mechanical insights have significant implications for device engineering in high-pressure or high-stress environments. The pressure-induced stiffening of GaAs enhances its suitability for pressure sensors, high-frequency devices, and components operating under harsh mechanical conditions. Meanwhile, the evolving ductility of InAs and InN beyond certain pressure thresholds points to their potential in flexible electronics, thermoelectric modules, and micro-/optoelectronic systems requiring both mechanical adaptability and durability. The central-force bonding nature and maintained ductility of GaN and InN under compression make them promising candidates for power electronics, LEDs, and aerospace applications. Overall, understanding these pressure-dependent elastic, anisotropic, and ductility behaviors informs optimal material selection, structural design, and future strategies for robust, adaptive semiconductor-based technologies under extreme mechanical conditions.

Anisotropic insight

The anisotropic character of a crystal provides important insight into its likely performance in different applications. Many material responses, for example fracture behavior, plastic deformation, phonon dispersion, and changes in chemical reactivity upon introduction of impurities are governed by the degree of mechanical anisotropy. We quantify anisotropy using several established indices and visualize it with two-dimensional maps of the elastic moduli. Figure 2S(a)–(d) presents 2D representations of Young's modulus, compressibility and shear modulus for GaAs, InAs, GaN and InN at 0, 6 and 14 GPa, generated using the ELATE code[73]. In an ideally isotropic material, three-dimensional representations of these moduli would appear perfectly spherical; deviations from this ideal shape indicate the degree of elastic anisotropy. As pressure increases, the materials deviate further from their ideal spherical shape, indicating that elastic properties become more direction-

dependent under compression, which may lead to uneven stress distribution and localized mechanical vulnerability along specific crystallographic directions.

Electronic properties

The classification of materials such as metallic, semiconducting, or insulation fundamentally relies on their electronic band structure, along with insights from the TDOS and PDOS[74], . These electronic characteristics are critical for comprehending the intrinsic physical and chemical nature of the compounds. To investigate the electronic behavior of GaAs, InAs, GaN, and InN, their band structures were computed along high-symmetry directions (W–L–Γ–X–W–K) within the first Brillouin zone under varying pressure, as summarized in Table S2. All four compounds band gaps progressively widen with increasing pressure illustrated in Fig. 10. This behavior may arise from pressure-enhanced orbital hybridization, which lowers the valence-band maximum and raises the conduction-band minimum, thereby driving a systematic band-gap expansion. The corresponding band structures of GaAs, InAs, GaN and InN at 0, 6, and 14 GPa are illustrated in Fig. 11(a-d), with the Fermi level fixed at 0 eV for consistency. The compounds preserved a direct band gap at the Γ-point across all applied pressures. However, pressure altered the relative dispersion of the conduction band, leading to subtle shifts in the positions of competing k-point minima. Although the Γ valley consistently remained the lowest-energy state, the neighboring conduction-band valleys moved closer in energy with increasing pressure, reflecting enhanced band reordering under compression. For GaAs as shown in Fig. 11(a), the direct band gap increases from 1.538 eV at ambient pressure to 2.0147 eV at 6 GPa, ultimately reaching 2.9682 eV at 14 GPa. In Fig. 11(b), InAs exhibits a narrower gap of 0.544 eV at 0 GPa that grows steadily, attaining 1.958 eV at 14 GPa. However, as shown in Fig. 11(c), GaN consistently retains a wide bandgap across all applied pressures, highlighting its potential for high-power and high-frequency device applications. At 0 GPa, the direct bandgap is 2.7493 eV, which further increases to 3.1937 eV at 14 GPa. Meanwhile the band structure of InN as depicted in Fig. 11(d) displays an initial gap of 0.458 eV, which increases to 0.8255 eV at 14 GPa, a range highly favorable for optoelectronic absorption and emission processes [The Expt. values of band gap are shown in Ref. 52, 63, 64]. The systematic widening of band gaps under compression highlights the tunability of these materials for pressure- or strain-engineered applications. Such control over the electronic structure is vital for optimizing semiconductors in next-generation photonic, sensing, and high-efficiency electronic devices.

The systematic widening of band gaps under compression highlights the tunability of these materials for pressure- or strain-engineered applications. Such control over the electronic structure is vital for optimizing semiconductors in next-generation photonic, sensing, and high-efficiency electronic devices. The electronic properties of GaAs, InAs, GaN, and InN were investigated through TDOS and PDOS, providing insights into the redistribution of electronic states under varying pressures. The TDOS was evaluated as shown in Fig. 12 at 0 to 14 GPa using both WIEN2k with the *mbjLDA* potential CASTEP. While CASTEP-based TDOS plots indicate some spurious states near the Fermi level, particularly under pressure, these are effectively eliminated in the WIEN2k results, affirming the clean semiconducting nature of the materials and reflecting consistency with the band structure calculations. As illustrated in Fig. 12(a-d), the value of TDOS for all four compounds vary smoothly with pressure.

Figure 13 (a–d) presents the PDOS for GaAs, InAs, GaN, and InN at selected pressures. There is rarely any change between 0 GPa and chosen pressure. As observed in Fig. 13(a), GaAs at 4 GPa, which is the pressure it has transitioned from brittle to ductile, the valence band is predominantly composed of As 4p states, while the conduction region is characterized by Ga 4p and minor 4s contributions. The orbital separation remains clear under pressure, with only mild redistribution across the band edges. In Fig. 13 (b-d) the PDOS graphs have been shown at 0 GPa and at the pressure of their possible phase transition to investigate if there is any visible change. In InAs from Fig. 13(b) at 8 GPa, As 4p and In 5p orbitals increasingly overlap, resulting in a denser conduction band region and subtle hybridization, which corresponds with the TDOS trends observed under pressure. According to Fig. 13(c), for GaN, evaluated at 6 GPa, the PDOS reveals strong N 2p participation in the valence band and Ga 4p states forming the conduction band. The clarity and spacing of these states support

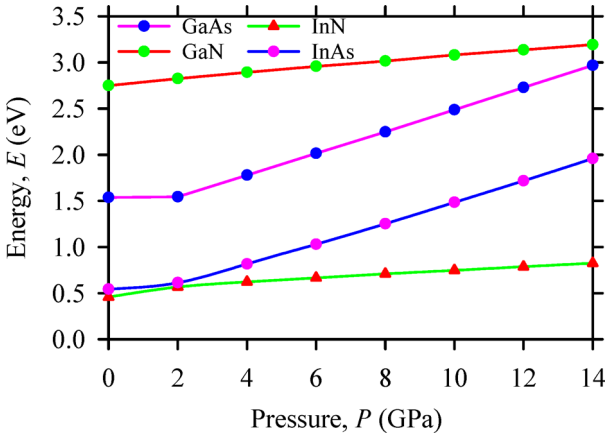

Fig. 10. Bandgap of GaAs, InAs, GaN and InN at various pressures.

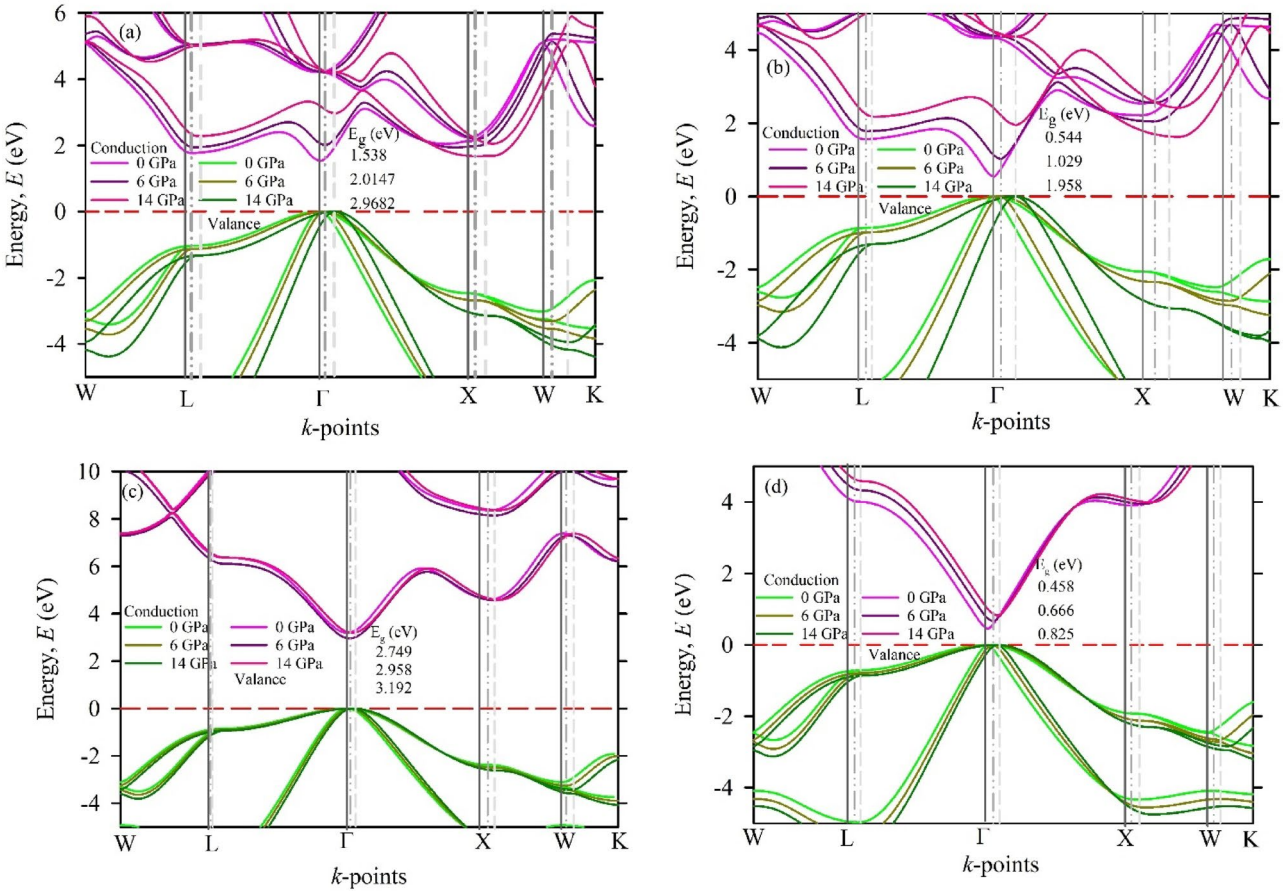

Fig. 11. The electronic band structure of **(a)** GaAs, **(b)** InAs, **(c)** GaN, **(d)** InN along with high symmetry direction in the Brillouin Zone at $P = 0$ GPa.

GaN's direct gap and its resistance to electronic distortion under strain. As depicted in Fig. 13(d), InN at 6 GPa, a noticeable redistribution of states is evident. The N 2p valence states remain dominant, but the conduction band shows a pronounced buildup of In 5p states, leading to band edge convergence and hinting at increased pressure sensitivity, consistent with TDOS observations.

Optical properties

The interaction of electromagnetic radiation with materials determines their optical behavior, which varies depending on the material's intrinsic properties. The evolution of optical properties under varying pressure conditions in these compounds is directly linked to their electronic structure. The dielectric function as a function of photon energy is expressed as,

$$\varepsilon(\omega) = \varepsilon_1(\omega) + i\varepsilon_2(\omega) \quad (3).$$

The complex dielectric function comprises $\varepsilon_1(\omega)$, the real part, and $\varepsilon_2(\omega)$, the imaginary part. The latter, $\varepsilon_2(\omega)$, arises from interbrand optical transitions and is computed using the momentum matrix elements, incorporating all possible electronic excitations from occupied to unoccupied states[75–78]. Using the Kramers-Kronig relationship[79–84], the real part $\varepsilon_1(\omega)$ of the dielectric function can be derived and from the complex dielectric function $\varepsilon(\omega)$, one can extract several fundamental optical parameters, including the absorption coefficient $\alpha(\omega)$, reflectivity $R(\omega)$, optical conductivity $\sigma(\omega)$, energy loss spectrum $L(\omega)$, refractive index $n_1(\omega)$, and extinction coefficient $n_2(\omega)$[76,77].

The optical properties of GaAs, InAs, GaN, and InN at 0, 6 and 14 GPa, covering photon energies up to 25 eV for polarization along the [100] direction, are presented in Fig. 14(a)–(d) and Fig. 15(a)–(d).

The optical absorption coefficient of XM (X = Ga, In; M = As, N), depicted in Fig. 14 (a), provides critical insights into the solar energy conversion efficiency of these materials by illustrating the penetration depth of specific light energies before absorption. As observed, all compounds exhibit zero absorption at low photon energy, indicating the absence of significant optical transitions in this range. This is followed by a small increase in absorption attributed to free carrier absorption, commonly referred to as Urbach absorption. For GaAs and InAs, the onset of significant absorption is observed near 4–5 eV, which is above their bandgap at 0 GPa. This behavior results from photon-induced electronic transitions from the valence band (VB) to the conduction band (CB). Notably, they both demonstrate a broader absorption spectrum at higher photon energies, with a pronounced absorption peak occurring around 6.3 eV. For GaN and InN, the absorption onset shifts significantly

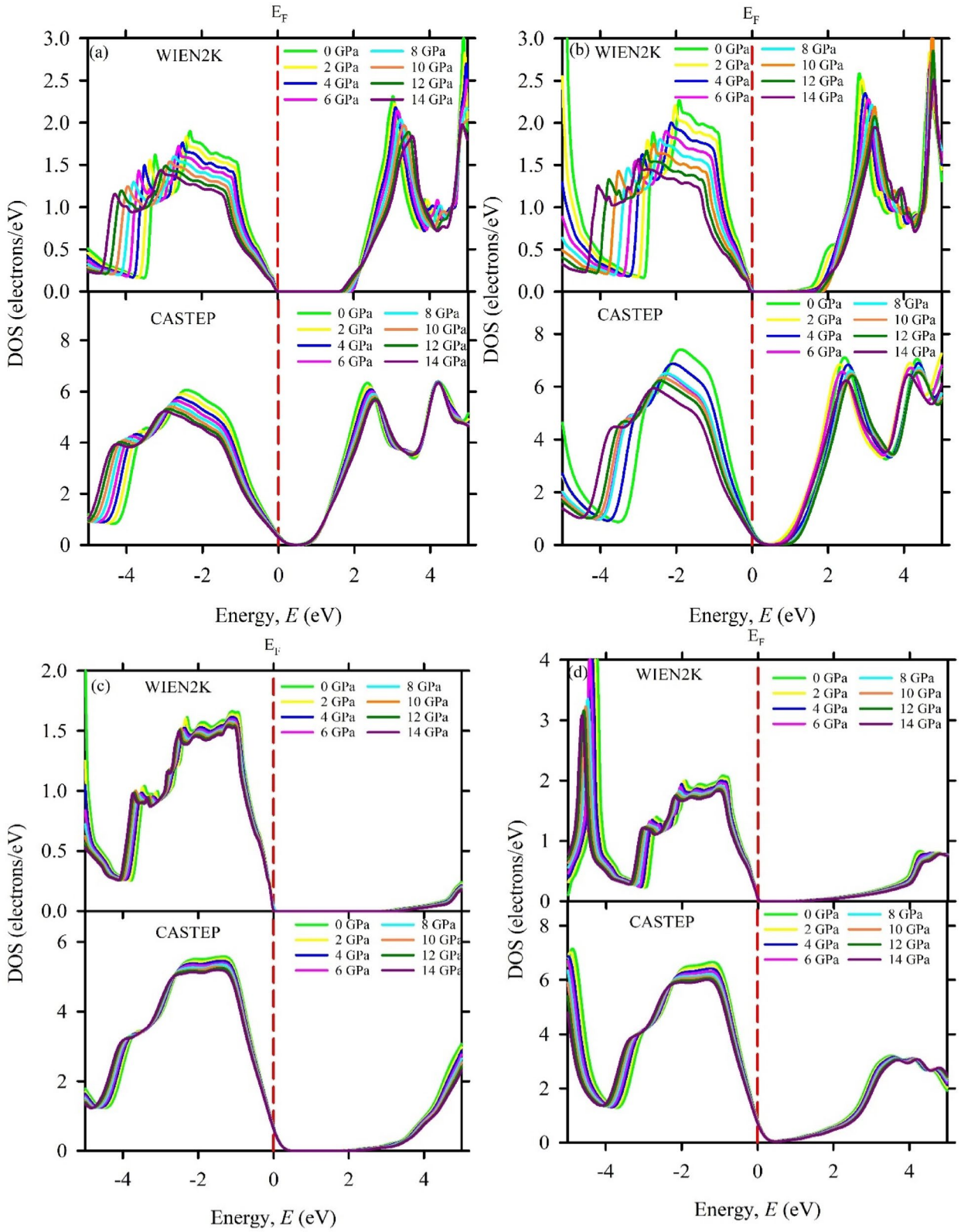

Fig. 12. Total density of state of **(a)** GaAs, **(b)** InAs, **(c)** GaN and **(d)** InN in WIEN2K and CASTEP under pressure.

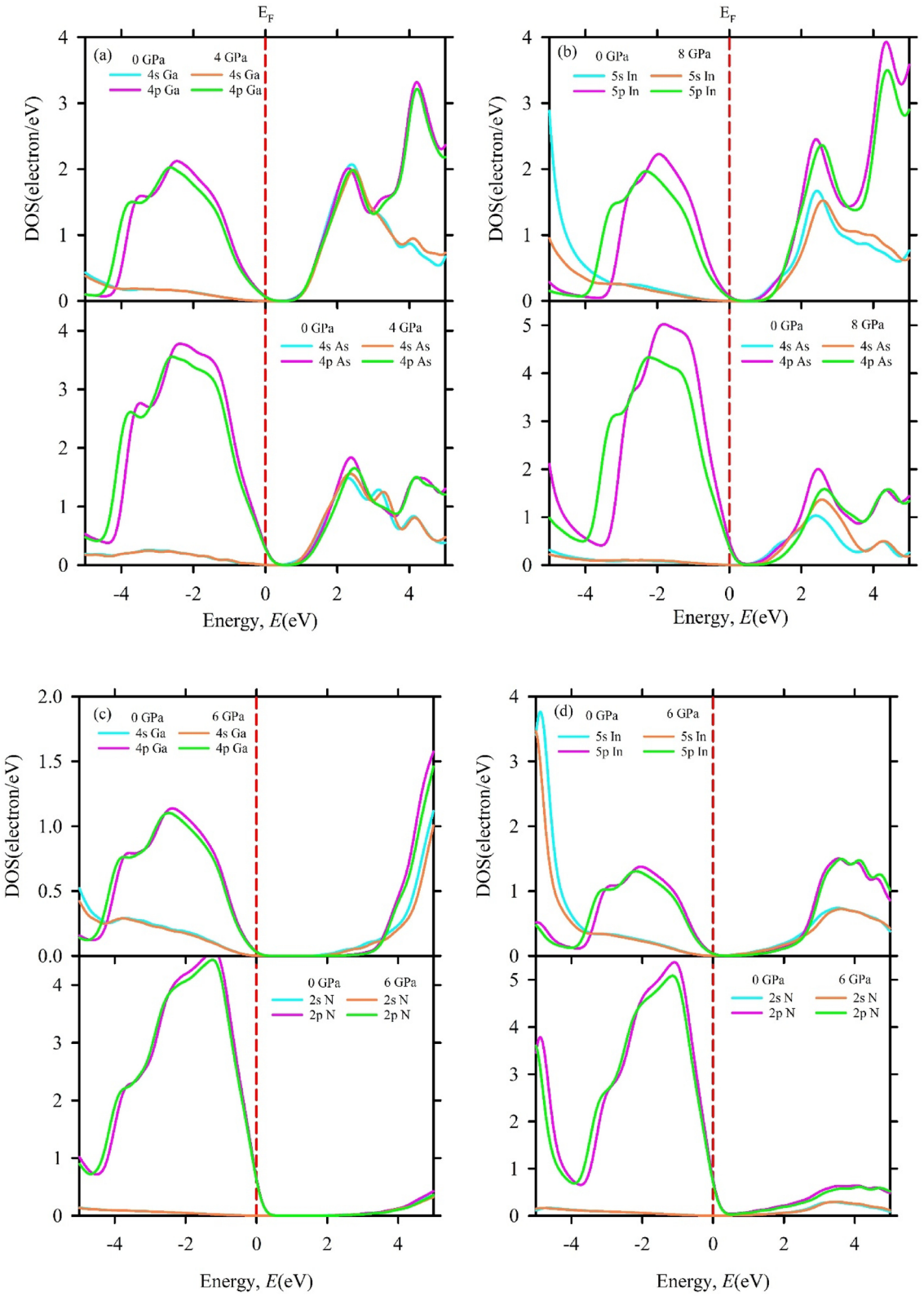

Fig. 13. The partial density of states of **(a)** GaAs at 0 and 4 GPa **(b)** InAs at 0 and 8 GPa **(c)** GaN at 0 and 6 GPa **(d)** InN at 0 and 6 GPa.

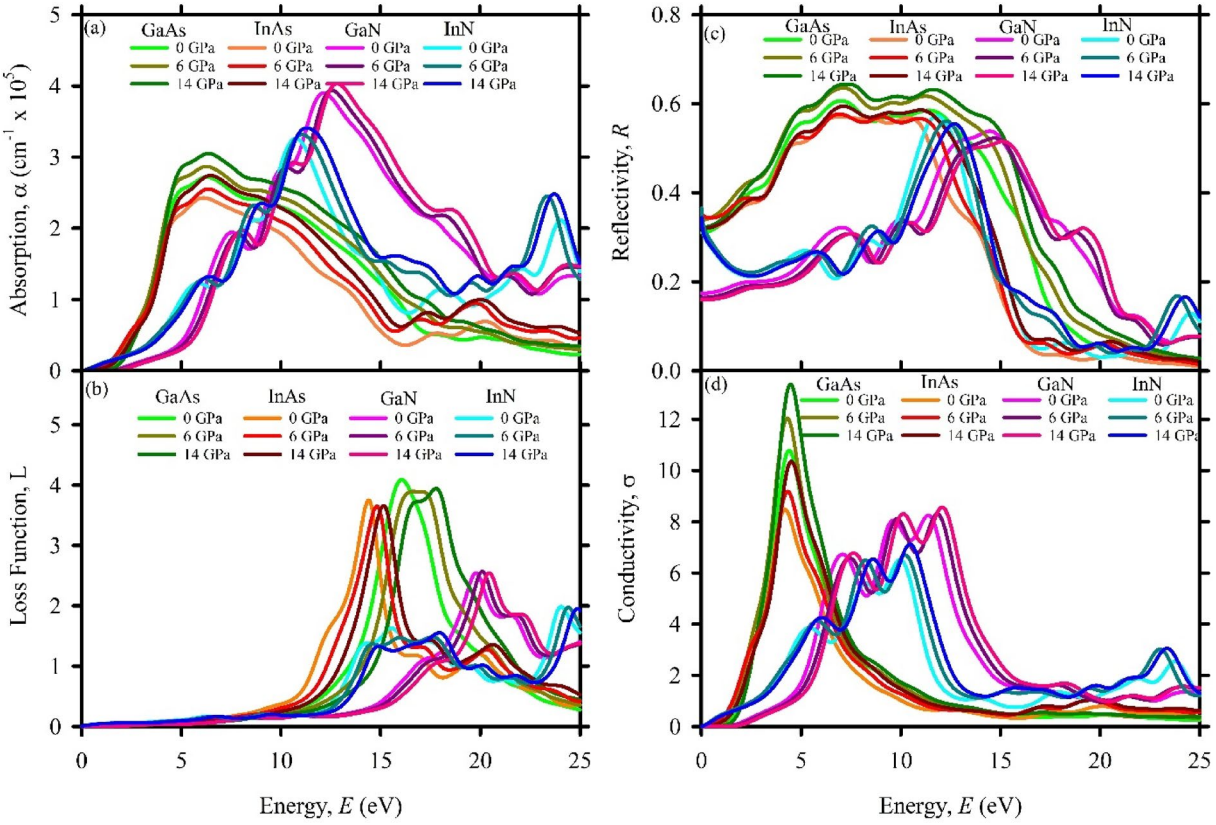

Fig. 14. At 0, 6 and 14 GPa **(a)** absorption **(b)** loss function, **(c)** reflectivity, and **(d)** conductivity of GaAs, InAs, GaN, and InN.

higher, peaking at around 10–12 eV, reflecting their potential utility in high-energy optical applications. For all the compounds the peak shifted higher as the pressures increased.

The energy loss function, as depicted in Fig. 14 (b), characterizes the energy dissipated by fast electrons traversing through GaAs, InAs, GaN, and InN. This function is directly linked to the material's dielectric properties and highlights the plasma resonance, identified by the plasma frequency ω_p, where the maximum energy loss occurs. For GaAs, the plasma frequency is observed at 16.46 eV at 0 GPa, indicating the characteristic energy at which collective oscillations of the electron cloud occur while InAs exhibits a slightly lower plasma frequency of 14.49 eV. On the other hand, GaN, displays the highest plasma frequency at 20.09 eV, while InN shows a plasma frequency of 15.40 eV, these variations in the plasma frequencies are pivotal for applications in plasmonic and high-frequency technologies. However, the peak of the loss function exhibited an inverse trend to that of absorption shifting to lower energies with increasing pressure.

The reflectivity spectra $R(\omega)$ of GaAs, InAs, GaN, and InN, as illustrated in Fig. 14 (c), reveal distinct optical behaviors. For GaAs and InAs, the reflectivity initially lies in the range of 0.31–0.32 and peaks at 0.58 under ambient pressure (0 GPa), indicating strong reflectance in the corresponding energy region. In contrast, GaN and InN exhibit slightly lower initial reflectivity values of 0.19 and 0.31, respectively, with peak values ranging between 0.53 and 0.58. At elevated pressures of 6 and 14 GPa, the reflectivity peaks for all compounds exhibit a slight upward shift, suggesting pressure-enhanced optical response. These high reflectivity peaks suggest potential applications in optical coatings, mirrors, and photonic devices operating within the relevant energy range.

The photoconductivity of these compounds reveals how effectively they generate charge carriers under photon excitation, highlighting their optoelectronic potential. As shown in Fig. 14 (d), for GaAs, photoconductivity begins at 1.1 eV, and peaks at 4.4 eV, where carrier generation is most efficient. InAs, with its narrower band gap, exhibits photoconductivity starting at 0.4 eV and reaching a maximum at 2.0 eV. GaN, shows photoconductivity onset at 2.0 eV and a peak at 9.6 eV, ideal for high-energy optical applications. In contrast, InN begins photoconductivity at 0.3 eV, with a maximum at 8.2 eV, demonstrating its broad energy range of carrier excitation. With increasing pressure (6 and 14 GPa), the photoconductivity peaks for all compounds shift more noticeably toward higher energies compared to reflectivity, indicating that pressure enhances interband transition thresholds. This upward shift implies improved tolerance to high-energy photon excitation, which is highly desirable for advanced optoelectronic and photonic devices operating under extreme conditions.

As observed in Fig. 15 (a) and (b), the dielectric properties of GaAs, InAs, GaN, and InN exhibit distinct trends in their real (ε_1) and imaginary (ε_2) parts, reflecting their unique electronic structures and optical transitions. Regarding GaAs, the real part increases smoothly up to 2.14 eV before sharply decreasing at 6.17 eV, followed

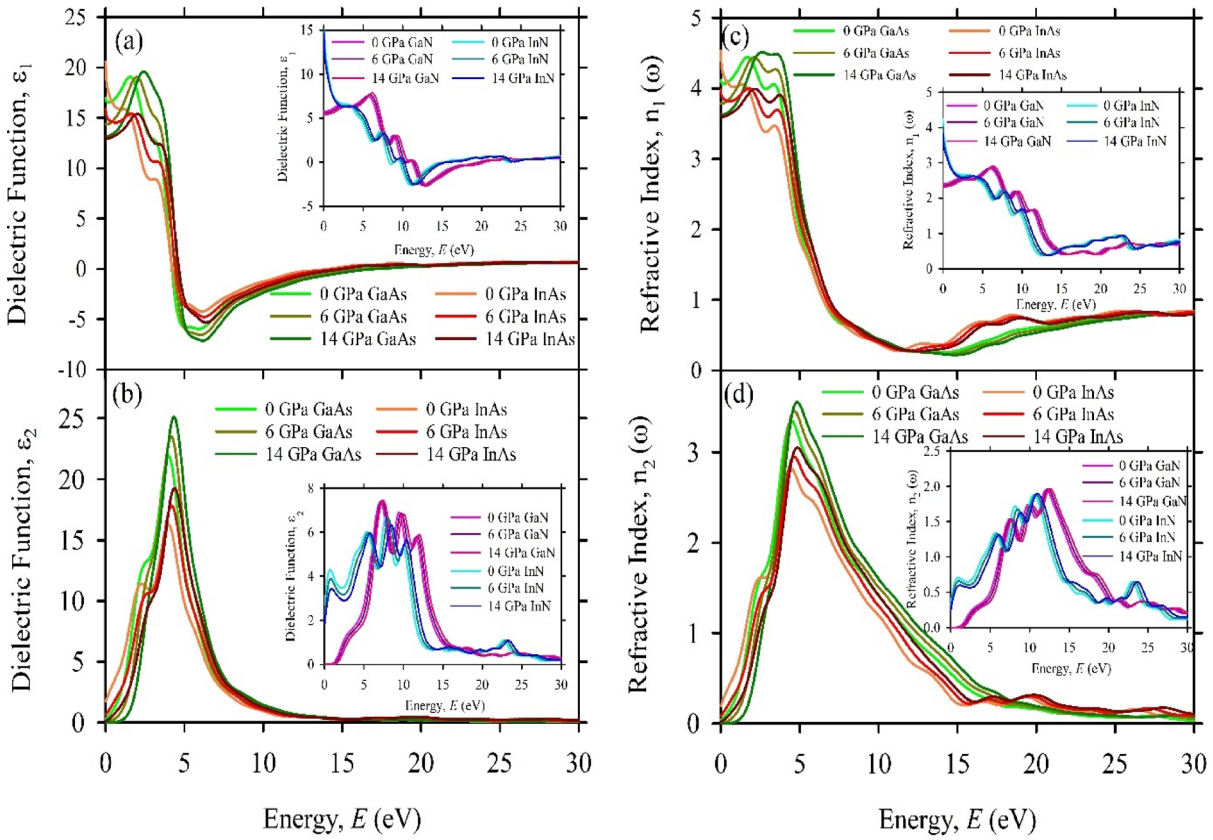

Fig. 15. The dielectric function **(a)**ε_1, **(b)**ε_2 and refractive index **(c)**n_1, and **(d)**n_2 for GaAs, InAs, GaN, and InN at 0, 6 and 14 GPa.

by a steady rise to 30 eV. The imaginary part begins at 0.6 eV, reaches a well-defined peak at 4.03 eV, and then gradually decreases, indicating a relatively simple and stable electronic transition process. Similarly, InAs shows comparable behavior, with the real part increasing to 1.77 eV, dropping to 6.01 eV, and then rising consistently. The imaginary part starts at 0.22 eV, peaks at 4.50 eV, and then diminishes gradually. These smooth variations in GaAs and InAs suggest fewer and more direct electronic transitions, resulting in a predictable optical response.

In contrast, GaN and InN display significantly more irregular dielectric behavior, characterized by frequent fluctuations. Concerning GaN, the real part increases up to 5.56 eV, decreases at 7.8 eV, rises again at 8.8 eV, and drops to its lowest point at 12.37 eV before showing a slight increase up to 30 eV. Similarly, the imaginary part shows sharp peaks and troughs, with a maximum at 6.87 eV and fluctuations persisting until 11.27 eV. InN also exhibits a similar pattern, with the real part starting high, decreasing sharply at 2.3 eV, fluctuating up to 10.7 eV, and then rising steadily. Its imaginary part peaks at 5.1 eV, shows discontinuities up to 12.5 eV, and decreases steadily afterward.

The dielectric behavior of GaAs and InAs reflects their stable and predictable electronic transitions, making them suitable for optoelectronic devices requiring consistent dielectric performance, such as modulators and waveguides. In contrast, the more complex transitions in GaN and InN suggest stronger interband interactions and higher-frequency dielectric responses, making them advantageous for high-frequency photonic and UV optoelectronic applications.

The refractive index $n_1(\omega)$ and extinction coefficient $n_2(\omega)$ provide key insights into the optical response of GaAs, InAs, GaN, and InN. High refractive indices in the ultraviolet region play a vital role in determining the efficiency of materials for applications such as photodetectors, solar cells, and other optoelectronic devices. A higher refractive index in this range signifies enhanced light-matter interaction, which is crucial for optimizing energy absorption and conversion. The refractive index spectra reveal that $n_1(\omega)$ exhibits an upward trend with increasing photon energy, particularly in the lower energy regime of the ultraviolet spectrum[78].

From Fig. 15 (c) and (d), it is apparent that, in the case of GaAs, $n_1(\omega)$ reaches a peak of 4.18 at 2.27 eV, while $n_2(\omega)$ attains a maximum value of 3.2 at 4.75 eV. Similarly, for InAs, $n_1(\omega)$ peaks at 3.85 at 1.96 eV, and $n_2(\omega)$ reaches 2.8 at 4.5 eV. Both materials exhibit smooth and predictable curves, indicating fewer complex transitions between energy states. This behavior is characteristic of their relatively simpler band structures, resulting in stable and efficient light propagation. In contrast, GaN and InN display more irregular patterns. For GaN, $n_1(\omega)$ peaks at 2.97 at 5.82 eV, while $n_2(\omega)$ reaches 2.01 at 11.99 eV. Similarly, for InN, $n_1(\omega)$ exhibits a sharp peak of 3.81 at 0.01 eV, with $n_2(\omega)$ achieving 1.9 at 10.53 eV.

At elevated pressures of 6 and 14 GPa, all compounds display a slight upward shift in the peaks of ε_1, ε_2, n_1, and n_2, reflecting the pressure-induced widening of the band gap and the consequent modification of interband transition energies. This enhancement implies improved dielectric strength and stronger light–matter interactions under compression, which is advantageous for tailoring these materials in high-performance optoelectronic and photonic applications operating under extreme conditions.

The graphs clearly reveal the unique optical properties of GaAs and InAs exhibit smoother profiles compared to the more fluctuating and irregular patterns observed for GaN and InN. This difference arises due to the nature of their electronic structures and optical transitions. For GaAs and InAs, smoother variations suggest fewer and more direct electronic transitions between energy bands, leading to less complexity in their optical responses. Their predictable loss and reflectivity minimize noise in devices. Conversely, GaN and InN display sharp and irregular peaks, indicating multiple overlapping transitions between energy bands, which can occur due to stronger excitonic effects in these materials. These fluctuations highlight the intricate interaction of photons with the electronic states of GaN and InN, resulting in more dynamic optical behavior. This distinction emphasizes the impact of electronic band structure on the optical properties of materials. Their sharp, fluctuating optical behavior suits high-energy applications like blue/UV LEDs, laser diodes, and high-frequency transistors. Their dynamic optical response is advantageous for wide-bandgap and high-power uses. Table 3 presents the static dielectric constants and static refractive index (real part), compared with previous studies to ensure reliability.

Thermal properties

In the present work, the Debye quasi-harmonic model is implemented to explore several thermodynamic properties of GaAs, InAs, GaN, and InN as a function of temperature and pressure. Using the given energy of these compounds as a function of molecular volume, the bulk modulus, Debye temperature, specific heats, volume thermal expansion coefficients, internal energy, and entropy are calculated with the help of the Gibbs program based on the Debye quasi-harmonic approximation[90]. The bulk modulus and Debye temperature of the given compounds in the temperature range from 0 to 1200 K at ambient pressure are shown in Fig. 16 (a and c) and at different pressures up to 20 GPa at 300 K in Fig. 13 (b and d). The bulk modulus (B) is a crucial parameter that quantifies the resistance of a material to uniform compression. As observed in Fig. 16(a), the bulk modulus at 0 GPa does not exhibit significant variation in the low-temperature regime ($T < 100$ K) but shows a linear decrease with increasing temperature, which is a characteristic behavior of semiconductors due to the anharmonic effects in the lattice vibrations. On the other hand, in Fig. 16(b), at a constant temperature of 300 K, the bulk modulus increases with rising pressure, indicating enhanced rigidity of the lattice under compression.

Similarly in Fig. 16(c), the Debye temperature (θ_D), which provides insight into the vibrational properties of a material, follows a comparable trend. The Debye temperature remains relatively stable at low temperatures but decreases with increasing temperature due to the thermal softening of the lattice vibrations. Conversely in Fig. 16(d), at a constant temperature of 300 K, θ_D increases monotonically with pressure, signifying an enhancement in the phonon frequencies, which can be attributed to the reduced interatomic spacing under compression. For GaAs and InN, θ_D increases from around 420.7 and 470 K respectively at 0 GPa to about 600 K at 20 GPa, whereas for InAs the value ranges from around from 320 K at 0 GPa to 490 K at 20 GPa. In contrast, GaN, the values range from about 763.7 K at 0 GPa to 906.0 K at 20 GPa. The higher θ_D values for GaN indicate stronger bonding and higher phonon frequencies, which contribute to its superior thermal conductivity.

The Grüneisen parameter (γ), which describes the anharmonic effects in lattice vibrations, is also shown in Fig. 17 (a & b). It is observed that γ decreases with increasing pressure, which is a typical behavior of semiconductors as compression reduces anharmonicity. For instance, in GaAs and InN, γ decreases from around 2.08 at 0 GPa to 1.62 and 1.88 respectively at 20 GPa, whereas in InAs and GaN, it declines from 2.20 to 2.02 and 1.71 respectively over the same pressure range. As observed in Fig. 17 (c), the thermal expansion coefficient (α), which quantifies the change in volume with temperature, exhibits an increasing trend with temperature up to a certain point, after which it saturates. It exhibits saturation around 300 K due to the anharmonic nature of lattice vibrations. At lower temperatures, phonon-phonon interactions are relatively weak, leading to a sharp increase in αv. However, as the temperature rises beyond 300 K, the phonon population increases, and the material approaches the classical limit where thermal expansion is governed by the Dulong-Petit law[90]. However, with increasing pressure in Fig. 17 (d), α decreases, suggesting that compressive forces restrict the thermal expansion of the lattice.

Finally, the specific heat capacities at constant volume (C_v) and constant pressure (C_p) for GaAs, InAs, GaN, and InN are displayed in Fig. 18 (a-d) as functions of temperature and pressure. The variations of C_v and

Compounds	ε_1	$n_1(\omega)$	Reference
GaAs	12.39	3.52	This work.
	12.40	3.26	[85]
InAs	13.59	3.69	This work.
	13.60	3.71	[86]
GaN	5.92	2.43	This work.
	8.9	2.30	[87,88]
InN	17.47	3.81	This work.
	15.30	3.05	[89]

Table 3. The static dielectric functions and static refractive indices of GaAs, InAs, GaN, and inn at 0 GPa.

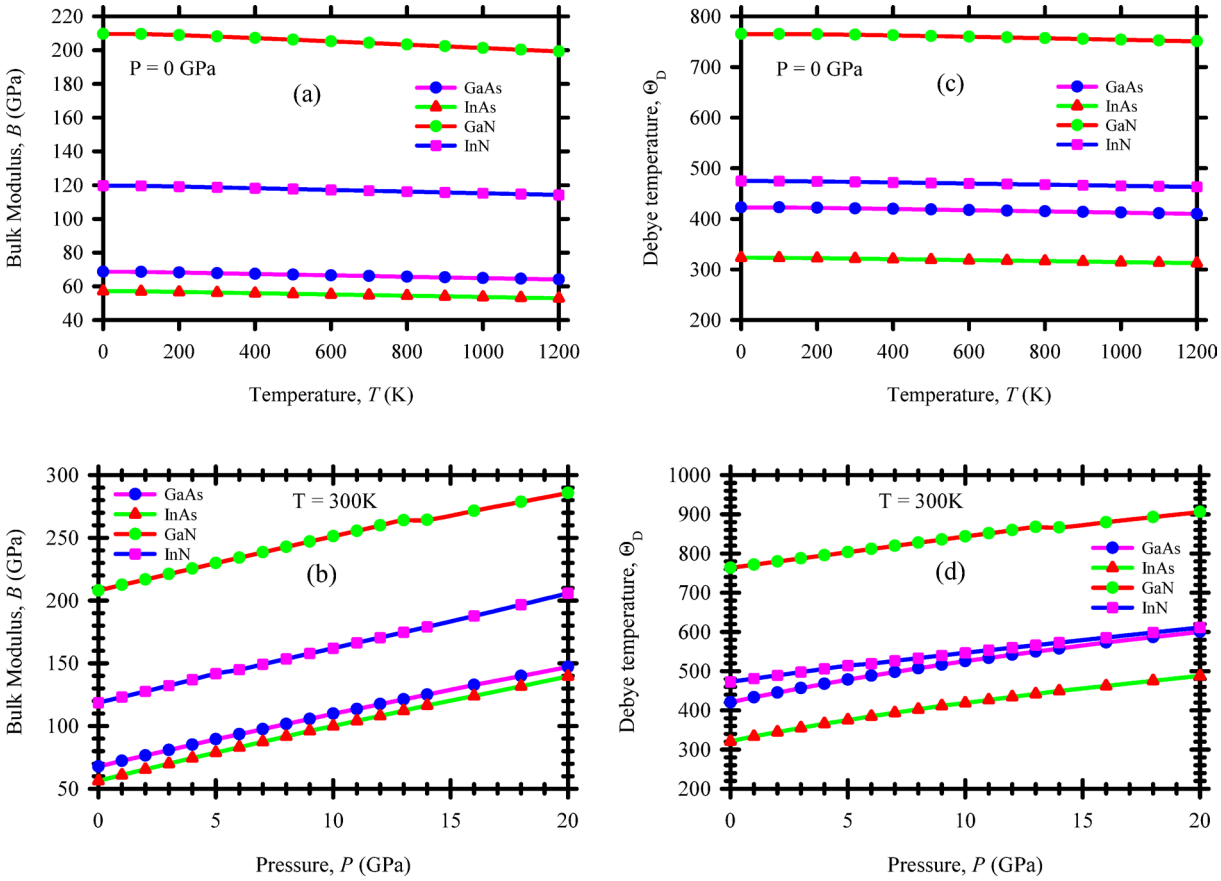

Fig. 16. The bulk modulus, B**(a)** temperature dependence, **(b)** pressure dependence and the Debye temperature, θ_D**(c)** variation with temperature, **(d)** and pressure for GaAs, InAs, GaN, and InN.

C_p with temperature as observed in Fig. 18 (a and b) follow the expected trends based on the Debye model. At low temperatures (T < 200 K), C_v and C_p exhibit a cubic dependence on temperature (T^3 law), which is characteristic of phonon-dominated heat capacity[92]. However, at higher temperatures (T > 300 K), both specific heats approach a constant value, following the Dulong–Petit law, which states that the molar heat capacity of a solid at high temperatures converges to 3nNkB[91]. For instance, C_v and Cp for GaAs increase initially but stabilize at around 45.3 J/mol·K and 45.7 J/mol·K, respectively, at higher temperatures. A similar behavior is observed for the other compounds, with GaN exhibiting slightly lower values due to its stronger bonding and higher Debye temperature.

The impact of pressure on C_v and C_p is relatively minor as we can see in Fig. 18 (c and d). As pressure increases, specific heat capacities decrease slightly, indicating reduced anharmonicity and restricted lattice vibrations. For example, in InAs, C_v and C_p at 0 GPa are 47.1 J/mol·K and 47.5 J/mol·K, respectively, but they decrease slightly to 43.9 J/mol·K and 44.0 J/mol·K at 20 GPa. This suggests that applying pressure stiffens the lattice, reducing the contribution of thermal vibrations to the heat capacity.

The melting temperature (T_m), and minimum thermal conductivity (K_{min}) of GaAs, InAs, GaN, and InN at 0–14 GPa are given in Table. S3. Among the four compound GaN has high melting point, 1528 K)and relatively large minimum thermal conductivity, 1.71 $W{\cdot}m^{-1}{\cdot}K^{-1}$, together with InN's robust, 1057 K at 0 GPa make them excellent choices for high-temperature, high-power and harsh-environment optoelectronic and RF devices where thermal durability and effective heat removal are critical. In contrast, the lower melting points of GaAs, 841 K and InAs, 716 K recommend them for moderate-temperature photonic and infrared applications or for thermoelectric/photonic devices that require careful thermal management or exploitation of lower thermal conductivity.

From the thermal property data, it is evident that materials like GaN and InN, characterized by high Debye temperatures and low thermal expansion coefficients, are well-suited for high-power and high-temperature electronic devices, where thermal stability and efficient heat dissipation are essential. The observed increase in bulk modulus and Debye temperature with pressure highlights their potential for high-pressure environments, such as space and deep-earth sensing applications. Additionally, the predictable variation of specific heat with temperature—and its slight decrease under pressure—makes these materials promising candidates for thermoelectric and thermal management systems. These thermal characteristics reflect strong lattice bonding and underscore the materials' robustness and reliability under extreme operating conditions.

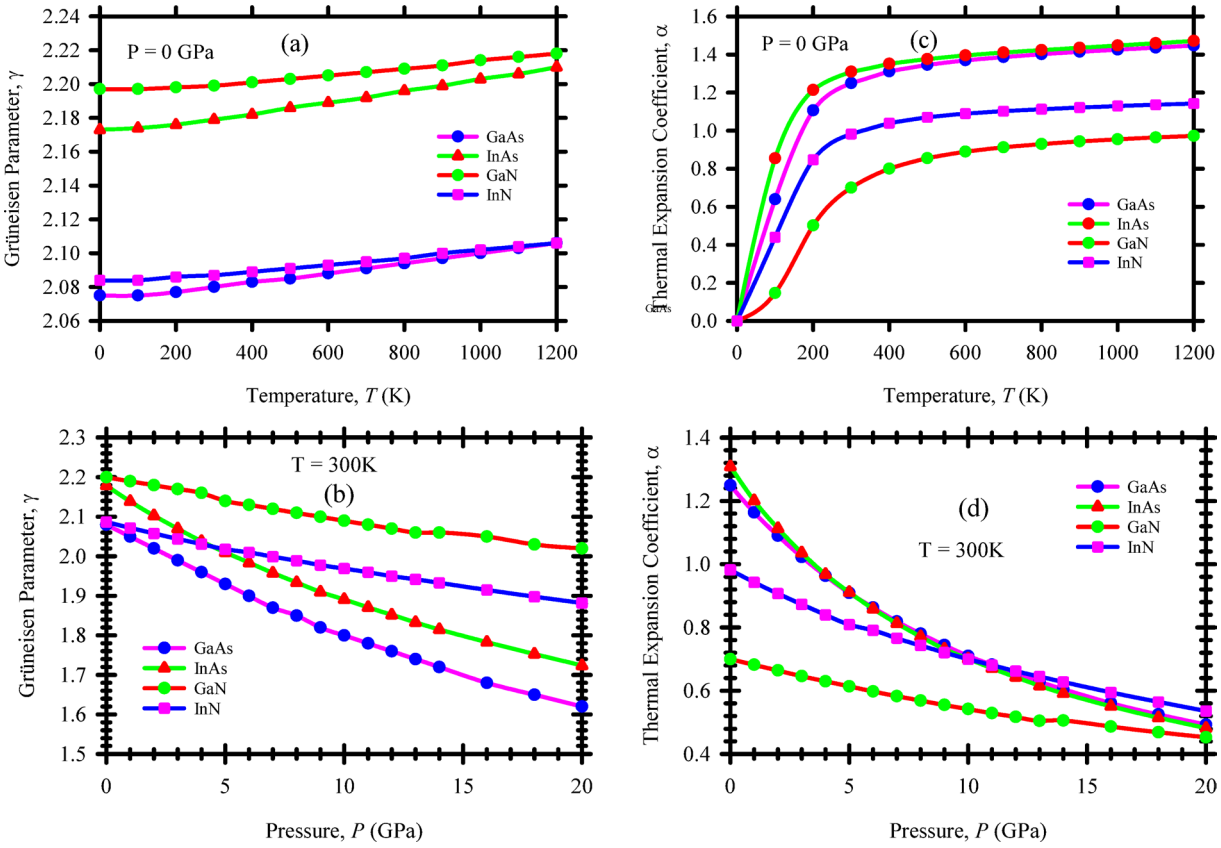

Fig. 17. The Grüneisen parameter γ, **(a)** temperature dependence, **(b)** pressure dependence and the thermal expansion coefficient, α **(c)** variation with temperature, **(d)** and pressure for GaAs, InAs, GaN and InN.

Conclusions

A comprehensive study about physical characteristics of Zinc blende materials *XM* (X = Ga, In and M = N, As) was explored via DFT CASTEP and WIEN2K approaches. This work's novelty stems from the systematic, cross-validated application of plane-wave and all-electron formalisms under hydrostatic compression, which yields a internally consistent dataset linking structural, vibrational, mechanical and electronic responses across multiple pressures. Dynamical constancy of these materials was assured from phonon calculations while the mechanical steadiness is ensured from stiffness constants. By correlating pressure-dependent phonon shifts with changes in elastic tensors and electronic structure, the study identifies mechanistic that underpin the observed property evolution. A consistent decrease in lattice parameters and volume with pressure reveals the increase in atomic bonding strength. Depending on pressure variations Pugh's ratio and Pettifor's values have changed which leads to brittle-to-ductile transition for GaAs. In contrast GaN was just below the ductile-brittle borderline and demonstrated anomalous elastic behavior under pressure for mechanical properties. Remarkably, the elastic constants experience pronounced shifts for In-based nitride and arsenide at in InN at 6 GPa, GaN 6 ± 2 GPa and InAs at 8 GPa, respectively. This behavior may lead possible pressure-driven phase transformation in crystal structure. Such pressure-triggered mechanical anomalies and transitions provide actionable design rules for strain- or pressure-engineered materials and motivate experimental high-pressure studies to validate predicted instabilities. The simulated bandgaps within the range of 0.4–3.1 eV, along with high dielectric constants make them ideal candidates for optoelectronic devices. Moreover, the demonstrated pressure-tunability of band gaps suggests practical pathways to tailor optical absorption and emission for adaptive photonic and sensing applications. Thermal property analysis revealed that specific heat capacities increase with temperature, following expected Debye behavior and approaching the Dulong–Petit limit at high temperatures. The low thermal expansion, mechanical strength, and pressure resilience of GaN, GaAs, InN and InAs, make them ideal for high power and harsh environment electronics, from electric vehicle power modules and RF amplifiers to aerospace and nuclear sensors. The combination of thermal durability and stable electronic performance under extreme conditions underscores their promise for next generation optoelectronic, thermoelectric, and power conversion platforms. Collectively, this integrated computational assessment supplies a rigorous materials-selection framework and predictive guidance for future device prototyping under non-ambient conditions.

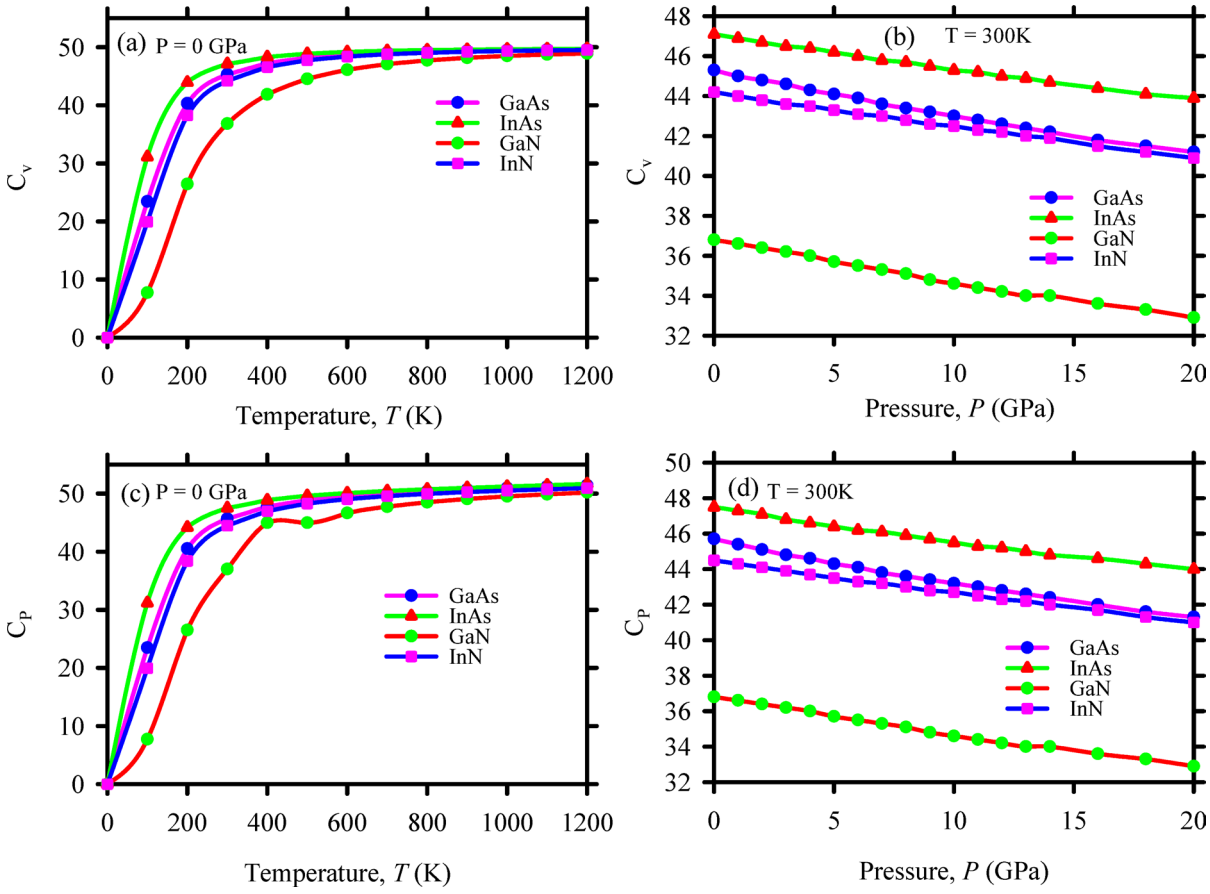

Fig. 18. The specific heat capacity at constant volume, C_v **(a)** temperature dependence, **(b)** pressure dependence and specific heat capacity at constant pressure C_p, **(c)** variation with temperature, **(d)** and pressure for GaAs, InAs, GaN and InN.

Data availability

The data will be available upon request to the corresponding author Md. Atikur Rahman ([atik0707phy@gmail.com](mailto: atik0707phy@gmail.com)) and Md. Shahajan Ali ([msali@pust.ac.bd](mailto: msali@pust.ac.bd))

Received: 24 August 2025; Accepted: 15 December 2025
Published online: 05 January 2026

References

1. Gupta, D. C. & Kulshrestha, S. Effect of high pressure on polymorphic phase transition and electronic structure of XAs (X = Al, Ga, In). *Phase Transitions*. **82** (12), 850–865 (2009).
2. Zheng, F. L., Zhang, J. M., Zhang, Y. & Ji, V. First-principles study of the perfect and vacancy defect AlN nanoribbon. *Phys. B: Condens. Matter*. **405** (17), 3775–3781 (2010).
3. Peng, F., Chen, D., Fu, H. & Cheng, X. The phase transition and the elastic and thermodynamic properties of aln: first principles. *Phys. B: Condens. Matter*. **403** (23–24), 4259–4263 (2008).
4. Kar, J. P., Bose, G. & Tuli, S. Influence of rapid thermal annealing on morphological and electrical properties of RF sputtered AlN films. *Mater. Sci. Semiconduct. Process*. **8** (6), 646–651 (2005).
5. Jackson, T. B., Virkar, A. V., More, K. L., Dinwiddie, R. B. Jr & Cutler, R. A. High-thermal-conductivity aluminum nitride ceramics: the effect of thermodynamic, kinetic, and microstructural factors. *J. Am. Ceram. Soc.* **80** (6), 1421–1435 (1997).
6. Feng, W., Cui, S., Hu, H., Zhao, W. & Gong, Z. Structural stability and optical properties of AlN explored by Ab initio calculations. *Phys. B: Condens. Matter*. **405** (2), 555–558 (2010).
7. Berolo, O., Woolley, J. C. & Van Vechten, J. A. Effect of disorder on the conduction-band effective mass, valence-band spin-orbit splitting, and the direct band gap in III-V alloys. *Phys. Rev. B*. **8** (8), 3794 (1973).
8. Kalvoda, S., Paulus, B., Fulde, P. & Stoll, H. Influence of electron correlations on ground-state properties of III-V semiconductors. *Phys. Rev. B*. **55** (7), 4027 (1997).
9. Klimeck, G., Bowen, R. C., Boykin, T. B. & Cwik, T. A. sp3s* Tight-binding parameters for transport simulations in compound semiconductors. *Superlattices Microstruct.* **27** (5–6), 519–524 (2000).
10. Wang, S. Q. & Ye, H. Q. Plane-wave pseudopotential study on mechanical and electronic properties for IV and III-V crystalline phases with zinc-blende structure. *Phys. Rev. B*. **66** (23), 235111 (2002).
11. Johnson, K. A. & Ashcroft, N. W. Corrections to density-functional theory band gaps. *Phys. Rev. B*. **58** (23), 15548 (1998).
12. Di Ventra, M. & Fernández, P. Semiconductor effective charges and dielectric constants in the tight-binding approach. *Phys. Rev. B*. **56** (20), R12698 (1997).

13. Khanin, D. V. & Kul'Kova, S. E. Electronic properties of III–V semiconductors. *Russ. Phys. J.* **48** (1), 70–77 (2005).
14. Geller, C. B. et al. Computational band-structure engineering of III–V semiconductor alloys. *Appl. Phys. Lett.* **79** (3), 368–370 (2001).
15. Wei, S. H. & Zunger, A. Band gaps and spin-orbit splitting of ordered and disordered al x Ga 1 – x as and Ga as x Sb 1 – x alloys. *Phys. Rev. B*. **39** (5), 3279 (1989).
16. Jansen, R. W. & Sankey, O. F. Ab initio linear combination of pseudo-atomic-orbital scheme for the electronic properties of semiconductors: results for ten materials. *Phys. Rev. B*. **36** (12), 6520 (1987).
17. Huang, M. Z. & Ching, W. Y. Calculation of optical excitations in cubic semiconductors. I. Electronic structure and linear response. *Phys. Rev. B*. **47** (15), 9449 (1993).
18. Wang, J. Q., Gu, Z. Q., Li, M. F. & Lai, W. Y. Intervalley Γ-X deformation potentials in III-V zinc-blende semiconductors by Ab initio pseudopotential calculations. *Phys. Rev. B*. **46** (19), 12358 (1992).
19. Holzapfel, W. B. Physics of solids under strong compression. *Rep. Prog. Phys.* **59** (1), 29 (1996).
20. Badding, J. V. High-pressure synthesis, characterization, and tuning of solid state materials. *Annu. Rev. Mater. Sci.* **28** (1), 631–658 (1998).
21. Ackland, G. J. High-pressure phases of group IV and III-Vsemiconductors. *Rep. Prog. Phys.* **64** (4), 483 (2001).
22. Vurgaftman, I. & Meyer, J. R. Band gap for III-V semiconductors. *J. Appl. Phys.* **94** (6), 3675–3696 (2003).
23. Mujica, A., Rubio, A., Munoz, A. & Needs, R. J. High pressure phases of group IV, III-V and II-VI compounds. *Rev. Mod. Phys.* **75** (3), 863–912 (2003).
24. Ali, M. S. & Pervin, R. *Phys. B* **673**, 415491. (2024).
25. Bylander, D. M. & Kleinman, L. Self-consistent energy bands and formation energy of the (GaAs)1(AlAs)1(001) superlattice. *Phys. Rev. B*. **34** (8), 5239–5242 (1986).
26. Greene, R. G. et al. *Phys. Rev. Lett.* **72**, 2045–2048. (1994).
27. Weir, S. T., Vohra, Y. K., Vanderborgh, C. A. & Ruoff, A. L. Structural phase transitions in GaAs to 108 GPa. *Phys. Rev. B*. **39**, 1280–1283 (1989).
28. Singh, R. K. & Singh, S. High-pressure phase transition and elastic behavior of aluminum compound semiconductors. *Phys. Rev. B*. **45**, 9411–9415 (1992).
29. Wei, S. H., Ferreira, L. G. & Zunger, A. First-principles calculation of temperature-composition phase diagrams of semiconductor alloys. *Phys. Rev. B*. **41**, 8240–8254 (1990).
30. Chetty, N., Munoz, A. & Martin, R. M. First-principles calculation of the elastic constants of alas. *Phys. Rev. B*. **40**, 11934–11937 (1989).
31. Besson, J. M. et al. High-pressure phase transition and phase diagram of gallium arsenide. *Phys. Rev. B*. **44**, 4214–4220 (1991).
32. Vohra, Y. K., Weir, S. T. & Ruoff, A. L. High-pressure phase transitions and equation of state of the III–V compound InAs up to 27 GPa. *Phys. Rev. B*. **31**, 734–738 (1985).
33. Yang, R. K., Zhu, C. S., Wei, Q. & Du, Z. A first-principles study of the properties of four predicted novel phases of AlN. *J. Phys. Chem. Solids*. **104**, 68–78 (2017).
34. Qin, H., Luan, X., Feng, C., Yang, D. & Zhang, G. Mechanical, thermodynamic and electronic properties of wurtzite and zinc-blende GaN crystals. *Materials* **10** (12), Article1419 (2017).
35. Wright, A. F. Elastic properties of zinc-blende and wurtzite AlN, GaN, and inn. *J. Appl. Phys.* **82** (6), 2833–2839 (1997).
36. Zhang, Z., Chai, C., Song, Y., Kong, L. & Yang, Y. A DFT study on physical properties of III–V compounds (AlN, GaN, AlP, and GaP) in the P3121 phase. *Mater. Res. Express*. **8**, 025908 (2021).
37. Bungaro, C., Rapcewicz, K. & Bernholc, J. Ab initio phonon dispersions of wurtzite AlN, GaN, and inn. *Phys. Rev. B*. **61** (10), 6720 (2000).
38. Kim, K., Kent, P. R. C., Zunger, A. & Geller, C. B. Atomistic description of the electronic structure of $In_xGa_{1-x}As$ alloys and InAs/GaAs superlattices. *Phys. Rev. B*. **66** (4), Article045208 (2002).
39. Pickett, W. E. Pseudopotential methods in condensed matter applications. *Comput. Phys. Rep.* **9** (3), 115–197 (1989).
40. Clark, S. J. et al. First principles methods using CASTEP. *Z. für Kristallographie*. **220** (5–6), 567–570 (2005).
41. Hohenberg, P. & Kohn, W. Inhomogeneous electron gas. *Phys. Rev.* **140** (A4), A1133–A1138 (1965).
42. Accelrys. *Materials Studio CASTEP manual* (pp. 261–262). Retrieved June 24, 2025, from (2010). http://www.tcm.phy.cam.ac.uk/castep/documentation/WebHelp/CASTEP.html
43. Perdew, J. P. & Wang, Y. Accurate and simple analytic representation of the electron-gas correlation energy. *Phys. Rev. B*. **45**, 13244–13249 (1992).
44. Lu, C., Miao, M. & Ma, Y. Structural evolution of carbon dioxide under high pressure. *J. Am. Chem. Soc.* **135** (38), 14167–14171 (2013).
45. Monkhorst, H. J. & Pack, J. D. Special points for Brillouin-zone integrations. *Phys. Rev. B*. **13**, 5188–5192 (1976).
46. Othman, M. S. Simulation mechanical properties of lead sulfur selenium under pressure. *J. Mod. Phys.* **4**, 185–190 (2013).
47. Othman, M. S. H. & Elkenany, E. B. Structural and optical properties of GaAs and InAs for doping Sb under the effect of pressure and temperature: DFT and EPM investigations. *Opt. Quantum Electron.* **54**, 807 (2022).
48. Segall, M. D. et al. First-principles simulation: Ideas, illustrations and the CASTEP code. *J. Phys.: Condens. Matter*. **14**, 2717–2744 (2002).
49. Refson, K., Tulip, P. R. & Clark, S. J. Variational density-functional perturbation theory for dielectrics and lattice dynamics. *Phys. Rev. B*. **73** (15), Article155114 (2006).
50. Blaha, P., Schwarz, K., Madsen, G. K. H., Kvasnicka, D. & Luitz, J. *WIEN2K: Full Potential Linearized Augmented Plane Wave and Local Orbitals Program for Calculating Crystal Properties* (Vienna University of Technology, 2001).
51. Tran, F. & Blaha Accurate band gaps of semiconductors and insulators with a semilocal exchange-correlation potential. *Phys. Rev. Lett.* **102** (22), Article226401 (2009).
52. Vurgaftman, I., Meyer, J. R. & Ram-Mohan, L. R. Band parameters for III–V compound semiconductors and their alloys. *J. Appl. Phys.* **89**, 5815–5875 (2001).
53. Koukaras, E. N., Kalosakas, G., Galiotis, C. & Papagelis, K. Phonon properties of graphene derived from molecular dynamics simulations. *Sci. Rep.* **5** (1), 12923 (2015).
54. Yun, Y., Legut, D. & Oppeneer, P. M. Phonon spectrum, thermal expansion and heat capacity of UO_2 from first-principles. *J. Nucl. Mater.* **426** (1–3), 109–114 (2012).
55. Kresse, G., Furthmüller, J. & Hafner, J. Ab initio molecular dynamics for liquid metals. *Europhys. Lett.* **32** (9), 729–734 (1995).
56. Parlinski, K., Li, Z. Q. & Kawazoe, Y. First-principles determination of the soft mode in cubic ZrO_2. *Phys. Rev. Lett.* **78** (21), 4063–4066 (1997).
57. Wang, J. & Zhou, Y. Dependence of elastic stiffness on electronic band structure of nanolaminate M_2AlC (M = Ti, V, Nb, and Cr) ceramics. *Physical Rev. B*, **69**(21), (2004). Article 214111-214120.
58. Wu, M. M., Wen, L., Tang, B. Y., Peng, L. M. & Ding, W. J. First-principles study of elastic and electronic properties of $MgZn_2$ and $ScZn_2$ phases in Mg–Sc–Zn alloy. *J. Alloys Compd.* **506** (1), 412–417 (2010).
59. Born, M. On the stability of crystal lattices. *Math. Proc. Cambridge Philos. Soc.* **36** (2), 160–172 (1940).
60. Mouhat, F. & Coudert, F. X. Necessary and sufficient elastic stability conditions in various crystal systems. *Phys. Rev. B*. **90**, 224104 (2014).

61. Gao, J., Liu, Q. J. & Tang, B. Elastic stability criteria of seven crystal systems and their application under pressure: taking carbon as an example. *J. Appl. Phys.* **133**, 135901 (2023).
62. Martienssen, W. & Warlimont, H. (eds) *Springer Handbook of Condensed Matter and Materials Data* (Springer, 2005).
63. Han, N. T., Dien, V. K., Chang, T. R. & Lin, M. F. Optical excitations of graphene-like materials: group III-nitrides. *Nanoscale Adv.* **5**, 5077–5093. https://doi.org/10.1039/d3na00306j (2023).
64. Şahin, H. et al. Monolayer honeycomb structures of group-IV elements and III–V binary compounds: First-principles calculations. *Phys. Rev. B*. **80**, 155453 (2009).
65. Voigt, W. *Lehrbuch Der Kristallphysik* (Teubner, 1928).
66. Reuss, A. Z. Berechnung der Fließgrenze von Mischkristallen auf Grund der Plastizitätsbedingung für einkristalle. *Z. für Angewandte Math. Und Mechanik*. **9** (1), 49–58 (1929).
67. Hill, R. The elastic behaviour of a crystalline aggregate. *Proc. Phys. Soc. London, Sect. A*. **65** (5), 349–354 (1952).
68. Zener, C. *Elasticity and Anelasticity of Metals* (University of Chicago Press, 1948).
69. Haines, J., Léger, J. M. & Bocquillon, G. Synthesis and design of superhard materials. *Annu. Rev. Mater. Sci.* **31**, 1–23 (2001).
70. Senkov, O. N. & Miracle, D. B. Generalization of intrinsic ductile-to-brittle criteria by Pugh and pettifor for materials with a cubic crystal structure. *Sci. Rep.* **11**, 4531 (2021).
71. Teter, D. Computational alchemy: the search for new superhard materials. *MRS Bull.* **23**, 22–27 (1998).
72. Jiang, X., Zhao, J. & Jiang, X. Correlation between hardness and elastic moduli of the covalent crystals. *Comput. Mater. Sci.* **50** (7), 2287–2290 (2011).
73. Romain Gaillac, P. & Pluton Coudert François-Xavier, ELATE: an open-source online application for analysis and visualization of elastic tensors. *J. Phys. :Condens Matter*. **28** (27), 275201 (2016).
74. Hu, W. C., Liu, Y., Li, D. J., Zeng, X. Q. & Xu, C. S. First-principles study of structural and electronic properties of C14-type Laves phase Al_2Zr and Al_2Hf. *Comput. Mater. Sci.* **83**, 27–34 (2014).
75. Jana, D., Sun, C. L., Chen, L. C. & Chen, K. H. Effect of chemical doping of Boron and nitrogen on the electronic, optical, and electrochemical properties of carbon nanotubes. *Prog. Mater. Sci.* **58** (5), 565–672 (2013).
76. Wooten, F. *Optical Properties of Solids* Vol. 52 (American, 1972).
77. Wang, G. et al. First-principles study on the electronic and optical properties of Sn_xGe_{1-x}. *Opt. Commun.* **283** (21), 4307–4309 (2010).
78. Korozlu, N., Çolakoğlu, K., Deligöz, E. & Çiftçi, Y. The structural, electronic and optical properties of $Cd_xZn_{1-x}Se$ ternary alloys. *Opt. Commun.* **284** (7), 1863–1867 (2011).
79. Yang, M. et al. *Optik*, **125**(1), 424–429. (2014).
80. Liu, Q. J. et al. *Opt. Mater.*, **35**(12), 2629–2635. (2013).
81. Anua, N. N. et al. Non-local exchange correlation functionals impact on the structural, electronic and optical properties of III–V arsenides. *Semicond. Sci. Technol.* **28** (10), 105015 (2013).
82. Pavesi, L. & Guzzi, M. Photoluminescence of $Al_xGa_{1-x}As$ alloys. *J. Appl. Phys.* **75** (10), 4779–4842 (1994).
83. Ghimire, K., Zhao, D., Yan, Y. & Podraza, N. J. Optical response of mixed Methylammonium lead iodide and formamidinium Tin iodide perovskite thin films. *AIP Adv.* **7** (7), 075108 (2017).
84. Degheidy, A. R. & Elkenany, E. B. Temperature and pressure dependence of the electronic and optical properties of GaxIn1 – xAsyP1 – y matching different substrates. *Phys. B: Condens. Matter*. **456**, 213–220 (2015).
85. Blakemore, J. S. Semiconducting and other major properties of gallium arsenide. *J. Appl. Phys.* **53** (10), R123–R181 (1982).
86. Aspnes, D. E. & Studna, A. A. Dielectric functions and optical parameters of si, ge, gap, gaas, gasb, inp, inas, and Insb from 1.5 to 6.0 Ev. *Phys. Rev. B.* **27** (2), 985 (1983).
87. Bougrov, V., Levinshtein, M., Rumyantsev, S. L. & Zubrilov, A. in *Properties of Advanced Semiconductor Materials*. (eds Levinshtein, M., Rumyantsev, S. L. & Shur, M. S.) (Wiley, 2001).
88. Barker, A. S. Jr. & Ilegems, M. Infrared lattice vibrations and free-electron dispersion in GaN. *Phys. Rev. B.* **7**, 743–750 (1973).
89. Zubrilov, A. Properties of Advanced Semiconductor Materials: GaN, AlN, InN, BN, SiC, SiGe (49–66). In (eds Levinshtein, M. E., Rumyantsev, S. L. & Shur, M. S.) Properties of Advanced Semiconductor Materials: GaN, AlN, InN, BN, SiC, SiGe. Wiley. (2001).
90. Debye, P. Zur theorie der Spezifischen wärmen. *Ann. Phys.* **344** (14), 789–839 (1912).
91. Petit, A. T. & Dulong, P. L. Study on the measurement of specific heat of solids. *Ann. Chim. Phys.* **10** (395), 629 (1819).
92. Blanco, M. A., Francisco, E. & Luana, V. G. I. B. B. S. GIBBS: isothermal-isobaric thermodynamics of solids from energy curves using a quasi-harmonic Debye model. *Comput. Phys. Commun.* **158** (1), 57–72 (2004).

Acknowledgements

A. Irfan extends his appreciation to the Deanship of Research and Graduate Studies at King Khalid University for funding this work through the Large Groups Research Project under grant number (RGP2/74/46).

Author contributions

Maahi Sabah (First author): Data analysis, Methodology, Data Curation, Writing original draft. Ahmad Irfan: Methodology, Data Curation, Funding Acquisition. Md. Saiful Islam: Data analysis. Md. Tanvir. Ahmed: Investigation, Methodology. Ruma Parvin: Writing-Review & Editing. Md. Atikur Rahman (corresponding Author): Writing-Review & Editing. Md. Shahajan Ali: (Corresponding Author) Conceptualization, Supervision, Review & Editing.

Declarations

Competing interests

The authors declare no competing interests.

Additional information

Supplementary Information The online version contains supplementary material available at https://doi.org/10.1038/s41598-025-33576-5.

Correspondence and requests for materials should be addressed to M.A.R. or M.S.A.

Reprints and permissions information is available at www.nature.com/reprints.

Publisher's note Springer Nature remains neutral with regard to jurisdictional claims in published maps and institutional affiliations.